JM

MET O 11 TECHNICAL NOTE NO 247

SOME EXPERIMENTS WITH TWO-DIMENSIONAL SEMI-GEOSTROPHIC AND PRIMITIVE EQUATION MODELS, WITH SIGMA AS THE VERTICAL COORDINATE

C A Parrett

Met O 11 (Forecasting Research)

Meteorological Office

London Road

Bracknell

Berkshire

England

February 1987

1. Introduction

This technical note describes some results from two two-dimensional atmospheric models used for research purposes in the Mesoscale Dynamics group in Met O 11. They are a semi-geostrophic (S.G.) model and a primitive equation (P.E.) model, with sigma as the vertical coordinate, and are extensions of the height-coordinate models mentioned in [1].

The S.G. model incorporates a different iteration procedure to the one described in [1]. This is because it was found in the frontal deformation case that the iteration used to calculate the cross-front ageostrophic flow was not converging well with the forward-backward scheme in use then. This was revealed by oscillations with a period of about 12 hours. The scheme was therefore changed to be backward-implicit, as in [2], solving for the ageostrophic stream-function by relaxation. This improved the convergence. The scheme and the full S.G. model are described in section 2.

The P.E. model (advective formulation) is described in section 3. A version of the model was written in flux form to achieve better conservation properties in the model [3], but in the presence of steep bottom topography as in [4] it became unstable after a few hours, despite increasing the horizontal diffusion coefficient and including vertical diffusion. This may be due to non-linear instabilities generated by having a small grid-length (O (10 km)). The formulation was essentially the same as in use in the Met O 20 GCM [5]. The form of the horizontal diffusion in the advective formulation presented here was chosen to maintain conservation of mass and momentum.

Section 4 describes a formulation of vertical diffusion, dependent on the local Richardson number, which was used in both models.

The results from two different cases are then presented in section 5, with a comparison of the models. The first case is similar to the frontal deformation case looked at in [1], but including a representation of the tropopause. The second case includes bottom topography in the form of a ridge and a realistic vertical profile of θ.

2. The semi-geostrophic model

The two-dimensional semi-geostrophic problem solved here can be written (following [1], [6] and [7]) as;-

definition of geostrophic wind: $$\frac{\partial \phi}{\partial x} + RT \frac{\partial}{\partial x}(\ln P_*) - f v_g = 0 \qquad (1)$$

y-momentum equation: $$\frac{\partial v_g}{\partial t} + (u_{ag} - \alpha x)\frac{\partial v_g}{\partial x} + \alpha v_g + \dot{\sigma}\frac{\partial v_g}{\partial \sigma} + f u_{ag} = \frac{K}{P_*}\frac{\partial}{\partial x}\left(P_* \frac{\partial v_g}{\partial x}\right) \qquad (2)$$

conservation of potential temperature, θ: $$\frac{\partial \theta}{\partial t} + (u_{ag} - \alpha x)\frac{\partial \theta}{\partial x} + \dot{\sigma}\frac{\partial \theta}{\partial \sigma} = \frac{K}{P_*}\frac{\partial}{\partial x}\left(P_* \frac{\partial \theta}{\partial x}\right) \qquad (3)$$

continuity equation: $$\frac{\partial P_*}{\partial t} + \frac{\partial}{\partial x}(u_{ag} P_*) - \alpha x \frac{\partial P_*}{\partial x} + \frac{\partial}{\partial \sigma}(\dot{\sigma} P_*) = 0 \qquad (4)$$

hydrostatic relation: $$\frac{\partial \phi}{\partial \sigma} + \frac{RT}{\sigma} = 0 \qquad (5)$$

Sigma (σ) is used as the vertical coordinate ($\sigma = \frac{P}{P_*}$).

Included in the above equations is a horizontal geostrophically balanced deformation field of the form $u = -\alpha x$, $v = \alpha y$; u_{ag} is the deviation from $u = -\alpha x$. This deformation field was used to produce frontogenesis in the first set of experiments to be described. The equations given are for the plane $y = 0$ and all variables used are independent of y. The only y variation is that of the basic state. In the second set of experiments α was set to zero. The equations also include horizontal diffusion of v_g and θ (with coefficient K), in a form which ensures mass and momentum conservation.

The lateral boundary conditions are

$$u_{ag} = 0 \text{ at } x = \pm e^{-\alpha t} L, \tag{6}$$

where 2L is the initial length of the model domain. The vertical boundary conditions are

$$\dot{\sigma} = 0 \text{ at } \sigma = 0, 1 \tag{7}$$

To solve the system of equations (1) to (7) they are split into an advection step and an adjustment step, similar to the procedure in [1]. It is convenient to calculate the vertical mean ageostrophic wind and surface pressure adjustment separately from the remainder of the ageostrophic wind which maintains thermal wind balance, by writing

$\underset{\sim}{u}_{ag} = \bar{\underset{\sim}{u}} + \underset{\sim}{u}^*$, where $\bar{\underset{\sim}{u}} = \bar{u}(x)$. The continuity equation (4) then naturally splits into:

$$\frac{\partial P^*}{\partial t} + \frac{\partial}{\partial x}(P^* \bar{u}) - \alpha x \frac{\partial P^*}{\partial x} = 0 \tag{8}$$

and $$\frac{\partial}{\partial x}(P_* u^*) + \frac{\partial}{\partial \sigma}(P_* \dot{\sigma}^*) = 0 \qquad (9)$$

For the adjustment step, which is carried out first, the vertically varying ageostrophic component of the flow is dealt with by solving auxiliary equations which calculate $\underset{\sim}{u}^*$ iteratively by advancing it a pseudo-time τ:

$$\frac{\partial u^*}{\partial \tau} = f v_g - \frac{\partial \phi}{\partial x} - RT \frac{\partial}{\partial x}(\ln P_*) \qquad (10a)$$

$$\frac{\partial v_g}{\partial \tau} = - f u^* - u^* \frac{\partial v_g}{\partial x} - \dot{\sigma}^* \frac{\partial v_g}{\partial \sigma} \qquad (10b)$$

$$\frac{\partial \theta}{\partial \tau} = - u^* \frac{\partial \theta}{\partial x} - \dot{\sigma}^* \frac{\partial \theta}{\partial \sigma} \qquad (10c)$$

P_* does not vary during this iteration.

With a physical time-step of Δt, it is necessary to integrate (10) for a pseudo time period $\Delta\tau$ of several times Δt in order to maintain sufficient accuracy in $\underset{\sim}{u}^*$. $\underset{\sim}{u}^*$ can be described by a stream-function τ defined by

$$P_* u^* = - \frac{\partial \psi}{\partial \sigma} \text{ and } P_* \dot{\sigma}^* = \frac{\partial \psi}{\partial x} \qquad (11)$$

with $\dot{\sigma}^* = 0$ at $\sigma = 0,1$, and $\int_0^1 u^* d\sigma = 0$. To incorporate this stream-function into (10), we multiply equation (10a) by P_* and take a backward time difference to obtain

$$(P_* u^*)^{\tau+\Delta\tau} = (P_* u^*)^{\tau} + \Delta\tau [P_* (f v_g - \frac{\partial \phi}{\partial x} - RT \frac{\partial}{\partial x}(\ln P_*))]^{\tau+\Delta\tau}$$

$$\text{or } (- \frac{\partial \psi}{\partial \sigma})^{\tau+\Delta\tau} = (- \frac{\partial \psi}{\partial \sigma})^{\tau} + \Delta\tau [P_* (f v_g - \frac{\partial \phi}{\partial x} - RT \frac{\partial}{\partial x}(\ln P_*))]^{\tau}$$

$$+ (\Delta\tau)^2 \frac{\partial}{\partial \tau} [P_* (f v_g - \frac{\partial \phi}{\partial x} - RT \frac{\partial}{\partial x}(\ln P_*))]^{\tau}$$

Now differentiating with respect to σ and using 5, 10(b) and 10(c) to give the time derivatives of v_g and θ we can extract a Poisson equation with variable coefficients:

$$A\left(\frac{\partial^2\psi}{\partial x^2}\right)^{\tau+\Delta\tau} + B\left(\frac{\partial^2\psi}{\partial\sigma^2}\right)^{\tau+\Delta\tau} = C \qquad (12)$$

where $A = -(\Delta\tau)^2 R\left(\frac{P_*}{P_o}\right)^{\kappa}\sigma^{\kappa-1}\left(\frac{\partial\theta}{\partial\sigma}\right)^{\tau}$

$$B = 1 + f^2(\Delta\tau)^2$$

and $$C = \left(\frac{\partial^2\psi}{\partial\sigma^2}\right)^{\tau} + \Delta\tau\frac{\partial}{\partial\sigma}\left[P_*\left(\frac{\partial\phi}{\partial x} + R\left(\frac{P_*}{P_o}\right)^{\kappa}\sigma^{\kappa}\theta\frac{\partial}{\partial x}(\ln P_*) - fv_g\right)\right]^{\tau}.$$

The remaining terms of the form $\frac{\partial}{\partial x}\left(\frac{\partial}{\partial\sigma}..\right)$ have been omitted in order to make equation (12) strongly elliptic; this leads to slow but safe convergence of the iteration. Inclusion of the other terms could lead to failure of the iteration. Equation (12) is discretised to the form

$$A\left(\psi_{i-1,j} - 2\psi_{i,j} + \psi_{i+1,j}\right)^{\tau+\Delta\tau}/\Delta x^2 + B\left(\psi_{i,j-1} - 2\psi_{i,j} + \psi_{i,j+1}\right)^{\tau+\Delta\tau}/\Delta\sigma^2 = C,$$

which is then solved by an inner iteration for $\psi_{i,j}$ ($\equiv \psi(i\Delta x, j\Delta\sigma)$) using a successive over-relaxation technique:

$$\psi^{r+1}_{i,j} = 0.66\left[A\left(\psi^{r+1}_{i-1,j} + \psi^{r}_{i+1,j}\right)/\Delta x^2 + B\left(\psi^{r+1}_{i,j-1} + \psi^{r}_{i,j+1}\right)/\Delta\sigma^2 - C\right]/\left[\frac{A}{\Delta x^2} + \frac{B}{\Delta\sigma^2}\right] - 0.32\psi^{r}_{i,j} \qquad (13)$$

where r is the iteration index. For the runs to be described later we iterated 40 times, which seemed to produce reasonably good convergence. The values of ψ are then used in (11) to obtain u^* and $\dot{\sigma}^*$, which are in turn used to advect M (= v_g+fx, the absolute momentum) and θ using centred space differencing as in the advection step below (15). A pseudo-time integration in τ for 10 time steps of 2000s was used for each physical timestep of

200s to iterate v_g and θ towards a balanced state. The physical values of u^* and $\dot{\sigma}^*$ are calculated by integrating over the pseudo-time iteration and scaling by the ratio $\Delta\tau/\Delta t$.

To ensure convergence of the iterative adjustment step, the vertical gradient of θ occurring in equation (12) must not be allowed to become too small. If it does, it is replaced by that of a reference profile. As is usual in semi- implicit schemes for operational forecast models, a reference θ-profile is used such that the temperature is constant with height.

The advection step (including the horizontal diffusion) then consists of solving

$$\left.\begin{aligned} \frac{\partial M}{\partial t} &= -(\bar{u} - \alpha x)\frac{\partial M}{\partial x} - \alpha M + \frac{K}{P_*}\frac{\partial}{\partial x}\left(P_*\frac{\partial M}{\partial x}\right) \\ \frac{\partial \theta}{\partial t} &= -(\bar{u} - \alpha x)\frac{\partial \theta}{\partial x} + \frac{K}{P_*}\frac{\partial}{\partial x}\left(P_*\frac{\partial \theta}{\partial x}\right) \end{aligned}\right\} \qquad (14)$$

and equation (8). These are solved numerically (for the $(n+1)^{th}$ time-step) by discretising to the form

$$M_{i,j}^{n+1} = M_{i,j}^{*} - \Delta t\left\{[(\bar{u}_i-\alpha x_i)(M_{i+1,j}-M_{i,j})+(\bar{u}_{i-1}-\alpha x_{i-1})(M_{i,j}-M_{i-1,j})]/2\Delta x+\alpha M_{i,j} + \frac{K}{P_{*i}}\left[\frac{1}{2}(P_{*i+1}+P_{*i})(M_{i+1,j}-M_{i,j}) - \frac{1}{2}(P_{*i}+P_{*i-1})(M_{i,j}-M_{i-1,j})\right]/\Delta x^2\right\}^{*} \qquad (15a)$$

$$\theta_{i,j}^{n+1} = \theta_{i,j}^{*} - \Delta t\left\{[(\bar{u}_i-\alpha x_i)(\theta_{i+1,j}-\theta_{i,j})+(\bar{u}_{i-1}-\alpha x_{i-1})(\theta_{i,j}-\theta_{i-1,j})]/2\Delta x + \frac{K}{P_{*i}}\left[\frac{1}{2}(P_{*i+1}+P_{*i})(\theta_{i+1,j}-\theta_{i,j}) - \frac{1}{2}(P_{*i}+P_{*i-1})(\theta_{i,j}-\theta_{i-1,j})\right]/\Delta x^2\right\}^{*} \qquad (15b)$$

$$P_{*i}^{n+1} = P_{*i}^{*} - \Delta t\left\{(\bar{u}_i-\bar{u}_{i-1})P_{*i} - \frac{1}{4}[(\bar{u}_i-\alpha x_i)+(\bar{u}_{i-1}-\alpha x_{i-1})](P_{*i+1}-P_{*i-1})\right\}^{*}/\Delta x \qquad (15c)$$

where $(...)^*$ denotes the value of $(...)$ after the iterative adjustment. $\bar{u}$ has to be calculated implicitly using the vertical mean of the geostrophic relation (1), the momentum equation (2) and the continuity equation (4). Because of the nonlinearity of this system, $\bar{u}$ is estimated from a linearised system in which v_g only depends on $\bar{u}$ through the Coriolis term. We can thus obtain the following equations:

$$[(\bar{v}_g^{\,o})^{n+1} - (\bar{v}_g^{\,o})^*]/\Delta t + f\bar{u}^{n+1} = 0 \qquad (16a)$$

$$\overline{\left[\frac{\partial \phi}{\partial x} + \frac{RT}{P_*}\frac{\partial P_*}{\partial x} - f v_g\right]}^{o\,n+1} = 0 \qquad (16b)$$

and $$(P_*^{n+1} - P_*^*)/\Delta t + P_*^{n+1}\left(\frac{\partial \bar{u}}{\partial x}\right)^{n+1} = 0 \qquad (16c)$$

Substituting for v_g and P_*^{n+1}, and using the linearised versions of (2) and (4), we obtain

$$\overline{\left(\frac{\partial \phi}{\partial x}\right)^* + \frac{RT}{P_*}\bar{n}^{+1}\left[\frac{\partial}{\partial x}\left(P_*^* + P_*^{n+1}\left(\frac{\partial \bar{u}}{\partial x}\right)^{n+1}\Delta t\right)\right] - f\left(v_g^* - f\bar{u}^{n+1}\Delta t\right)}^{o} = 0$$

$$\text{or } \overline{\left(\frac{\partial \phi}{\partial x} + RT\frac{\partial}{\partial x}(\ln P_*) - f v_g\right)^{*o}} + \Delta t\left(RT\frac{\partial^2 \bar{u}}{\partial x^2}\right)^{n+1} - f^2 \Delta t \bar{u}^{n+1} = 0 \qquad (17a)$$

Equation (17a) can then be discretised to the following form and solved for $\bar{u}$ by iterating to convergence:

$$\left(\bar{u}_i^{r+1} + \frac{1}{3}\bar{u}_i^{r}\right)\left(2\overline{RT}_i^{\,o}\,\Delta t/\Delta x + f^2\Delta t\right) = \frac{4}{3}\overline{RT}_i^{\,o}\left(\bar{u}_{i-1}^{r+1} + \bar{u}_{i+1}^{r}\right)\Delta t/\Delta x^2 - \left(\frac{\partial \phi}{\partial x} + RT\frac{\partial}{\partial x}(\ln P_*) - f v_g\right)_i^* \qquad (17b)$$

where r is the iteration index. The value of $\bar{u}$ obtained from (17b) is then used in the advection step (15) to update M, θ and P_*.

Care has to be taken in choosing initial data for the semi-geostrophic model so that the potential vorticity (q) is positive and values of θ increase upwards along lines of constant M; otherwise the implicit equation for the stream function becomes hyperbolic in some regions and the solution would be unstable to slantwise convection. To ensure that the θ-profile remains statically stable a simple convective adjustment is included in the model (implemented prior to each adjustment step). This is applied to each column and instantly mixes any statically unstable layers to produce a slightly stable profile while conserving θ. No adjustment to v_g was found necessary in the problems solved in this paper.

The grid used in the S.G. model and the P.E. model is shown in figure 1. The potential temperature (θ) and along-front/mountain wind (v) are stored in the centre of each grid-box; the cross-domain wind (u) is stored on the sides of the box, and the vertical velocity ($\dot{\sigma}$) is stored at the top and bottom of each grid-box.

3. The primitive equation model

The equations for the deformation problem studied in section 2 can be written as

$$\frac{\partial u}{\partial t} + \frac{1}{2}\frac{\partial}{\partial x}(u^2) + \dot{\sigma}\frac{\partial u}{\partial \sigma} + \frac{\partial \phi}{\partial x} + RT\frac{\partial}{\partial x}(\ln P_*) - fv = \frac{K}{P_*}\frac{\partial}{\partial x}\left(P_*\frac{\partial u}{\partial x}\right) \qquad (18)$$

$$\frac{\partial M}{\partial t} + (u-\alpha x)\frac{\partial M}{\partial x} + \dot{\sigma}\frac{\partial M}{\partial \sigma} = \frac{K}{P_*}\frac{\partial}{\partial x}\left(P_*\frac{\partial M}{\partial x}\right) \qquad (19)$$

$$\frac{\partial\theta}{\partial t} + (u-\alpha x)\frac{\partial\theta}{\partial x} + \dot{\sigma}\frac{\partial\theta}{\partial\sigma} = \frac{K}{P_*}\frac{\partial}{\partial x}\left(P_*\frac{\partial\theta}{\partial x}\right) \qquad (20)$$

$$\frac{\partial P_*}{\partial t} + \frac{\partial}{\partial x}(P_* u) - \alpha x\frac{\partial P_*}{\partial x} + \frac{\partial(P_*\dot{\sigma})}{\partial\sigma} = 0 \qquad (21)$$

$$\frac{\partial\phi}{\partial\sigma} + \frac{RT}{\sigma} = 0 \qquad (22)$$

The variables are again independent of y and the deformation field has been included such that the total cross-domain wind is u-αx (ie u here corresponds to u_{ag} in section 2). The boundary conditions are

$$\begin{aligned} u &= 0 \text{ at } x = \pm\left(L - \frac{\Delta x}{2}\right) \\ v &= 0 \\ \frac{\partial\theta}{\partial x} &= 0 \qquad \text{at } x = \pm L \\ \frac{\partial P_*}{\partial x} &= 0 \end{aligned} \qquad (23)$$

and $\dot{\sigma} = 0$ at $\sigma = 0, 1$.

These equations are integrated forward in time using a simple centred (or 'leap-frog') scheme, and discretised to the following form:

$$\delta_t \bar{u}^{t} = -\frac{1}{2}\delta_{2x}(u^2) - \overline{\dot{\sigma}^{x}\delta_\sigma u}^{\sigma} - \delta_x\phi - R\overline{\left(\frac{P_*}{P_o}\right)^{\kappa}\theta}^{x}\delta_x(\ln P_*) + f\bar{v}^{x} + K\overline{P_*^{-1}}^{x}\delta_x(P_*\delta_x u) \qquad (24)$$

$$\delta_t \bar{M}^{t} = -\overline{(u-\alpha x)\delta_x M}^{x} - \overline{\dot{\sigma}\delta_\sigma M}^{\sigma} + K P_*^{-1}\delta_x(\bar{P_*}^{x}\delta_x M) \qquad (25)$$

$$\delta_t \bar{\theta}^{t} = -\overline{(u-\alpha x)\,\delta_x\theta}^{x} - \overline{\dot{\sigma}\,\delta_\sigma\theta}^{\sigma} + K P_*^{-1}\delta_x(\bar{P_*}^{x}\delta_x\theta) \qquad (26)$$

$$\delta_t \bar{P_*}^{t} = -\delta_x(\bar{P_*}^{x}\tilde{u}) \qquad (27)$$

where $\tilde{u} = \frac{1}{N}\sum_{j=1}^{N} u_j$,

$$\dot{\sigma}_j = - P_*^{-1} \left(\delta_t \overline{P_*}^{t} \sigma_j - \Delta\sigma \sum_{N}^{j} \delta_x (P_* u)\right) \qquad (28)$$

and $\delta_\sigma \phi = - \overline{[R \left(P_*/P_O\right)^{\kappa} \theta]/\sigma}^{\sigma}$; (29)

where the standard notation $\delta_x u = (u(x + \frac{\Delta x}{2}) - u(x - \frac{\Delta x}{2}))/\Delta x$,

and $\overline{u}^{x} = (u(x - \frac{\Delta x}{2}) + u(x + \frac{\Delta x}{2}))/2$ has been used.

The vertical grid-spacing is uniform in σ, with $\Delta\sigma = \frac{1}{N-1}$, where N is the number of model levels in the vertical.

In order to prevent grid-splitting with the leap-frog time integration scheme, a time filter is applied to all the dependent variables. It is of the form

$$\theta^n = (1-\beta)\, \theta^{n'} + \frac{\beta}{2} (\theta^{n-1} + \theta^{n+1'}) \qquad (30)$$

where $\theta^{n'}$ is θ at timestep n before being filtered. The value of β was kept at 0.05 for the results shown here.

Unlike the S.G. model (equation (6)), exact lateral boundary conditions giving a well-posed problem do not exist for the P.E. model. Therefore a region of high horizontal diffusion is included near the boundaries, increasing linearly towards the boundaries, to produce a shear zone and allow the interior solution to decouple from that at the boundaries. Similarly, a zone of increased diffusion was applied near the upper boundary in some experiments, to prevent spurious reflections of wave energy.

The same simple convective adjustment as used in the S.G. model is included in the P.E. model. It is applied every 10 timesteps, at the same times as in the S.G. model.

4. Vertical diffusion

Vertical diffusion is applied (in the 'ridge' case) in the same form to both the S.G. and P.E. models, at the end of each main timestep. The scheme is based on that used in the UK operational model's boundary layer scheme [8]. It takes the form

$$\frac{\partial \theta}{\partial t} = \frac{\partial}{\partial z} \left(K_\theta \frac{\partial \theta}{\partial z} \right) \qquad (31)$$

where $K_\theta(z)$ is the diffusion coefficient given by

$$K_\theta = \lambda \, f_\theta(R_i) \left| \frac{\partial u}{\partial z} \right| ;$$

$$R_i = \frac{g}{\theta_o} \left| \frac{\partial \theta / \partial z}{\partial u / \partial z} \right|^2 \text{ is the local Richardson number,}$$

and $f_\theta(R_i) = \begin{cases} (1-16\,R_i)^{3/4} , & R_i \leq 0 \text{ (unstable)} \\ \exp(-3Ri), & R_i > 0 \text{ (stable).} \end{cases}$

Similar equations are used for v and u, except that $f_{v,u}(R_i) = (1-16\,R_i)^{1/2}$ for $R_i \leq 0$. This formulation assumes a constant mixing length of 100 m throughout the model, and the dependence on R_i ($f(R_i)$) has been chosen to remove areas where $R_i < {}^1/_4$ more effectively than with the operational boundary layer scheme.

5. Results

(a) Deformation front case

The initial data for this case is similar to that used in the final case shown in [1], but altered to be somewhat more realistic. It is shown in Figures 2 and 3; and the results up to 12 hours into the integrations, with a deformation rate (α) of 2×10^{-5} s^{-1}, are shown in Figures 4 to 11. All the figures show the lowest 12 km of the model domain and the fields have been interpolated from the model sigma levels onto height as the vertical coordinate. Figures 4 to 7 show the effect of the inward-moving boundaries in the S.G. model. There were 20 levels in the models for this case, and 200 grid points across the domain of length 2000 km.

Generally, there seem to be less differences at the front between the two models here than is seen in the results shown in [1]. Comparing the fields shown in Figures 4 to 7 with those in Figures 8 to 11, the overall frontal slope is slightly greater in the S.G. model and generally the front is a more distinct feature in this model. This better definition is probably due to the S.G. model requiring less horizontal diffusion than the P.E. model to prevent the fields becoming too rough and the model 'blowing-up' ($K = 500$ m^2 s^{-1} in the S.G. model compared with $K = 6250$ m^2 s^{-1} in the P.E. model). There is a little noise in the S.G. model's u and w fields (Figures 6 and 7) on the warm side of the front.

The largest difference at 12 hours is to the right (the warm side) of the front where there is a bulge in the isentropes of the P.E. model, associated with a minimum and maximum in the vertical velocity field (Fig 11 (b)). This feature was noticeable earlier at 6 hours (Fig 11 (a)) as a maximum of vertical velocity extending vertically throughout the model's troposphere, superimposed on the larger scale cross-frontal circulation with its sloping up- and down-drafts. There is little sign of this vertically-orientated region of upward motion in the results from the S.G. model (Fig. 7). Instead, the surface front is stronger, with the isentropes packed closely together at the surface (Fig. 4) and with an associated stronger shear zone (Fig. 5). Also, there is a region of strong upward motion in the warm air centred much closer to the surface, and the area of descent on the cold side of the front is centred higher up near to the model's tropopause.

(b) Mountain ridge case

Figure 12 shows the initial data used in this case: simply a stably stratified potential temperature (θ) field including a representation of the stratosphere, which is horizontally uniform, with an infinitely long mountain ridge in the centre-right of the domain. This θ field has been interpolated from constant height levels onto the model sigma-levels using a cubic spline. For plotting the cross-sections the fields are interpolated back to height levels. The along-mountain wind (v) was set to zero, but a cross-mountain wind of 10 ms^{-1} was simulated by moving the mountain to the left (by updating $\phi*$ in the models). The mountain was started-off moving very slowly and gradually increased in speed to 10 ms^{-1}

after $^1/_2$ hour, to reduce the formation of transient gravity waves, which would be excited by an impulsive start. In this case there were 40 levels in the models, and 100 grid-points across the 2000 km length of the domain. The mountain is of simple cosine shape, of height 1.3 km and half-wdith 3000 km. So, the Rossby number for this case ($R_o = {}^U/_{fL}$) is $^1/_3$, based on the half-width of the mountain. The horizontal diffusion coefficients for this case were K = 1000 m^2s^{-1} in the S.G. model and K = 20000 m^2s^{-1} in the P.E. model.

The fields after 24 hours of integration are shown in Figures 13 to 22. Common to both models, one can see a "start vortex" produced where the mountain was positioned initially, consisting of a dip in the isentropes (Figs. 13 and 18) and a cyclonic vortex with its maximum amplitude at the surface (Figs. 14 and 19). This is caused by the expansion of the column of atmosphere above the mountain initially, and the conservation of absolute vorticity. Compression of the air flowing over the mountain has similarly led to a positive vortex being formed above the mountain.

More interesting is the S.G. model's representation of the flow over the mountain. The lowest isentropes have been compressed slightly above the mountain with an associated strong cross-mountain flow (maximum ~ 22 ms^{-1}) very close to the surface at the mountain peak (Fig. 15). This acceleration over the mountain peak has led to upslope motion on the windward and downslope motion on the leeward slopes being confined to low levels over the mountain, with little or no disturbance away from the mountain (Fig. 16).

This result contrasts greatly with the results from the P.E. model (Figs. 18 to 22), where there is a great amount of wave activity above and downstream of the mountain. The cross-mountain flow (Figs. 20 and 21) near the surface exhibits a strong downslope wind with a maximum speed of 23 m s^{-1}, which decreases to 2 m s^{-1} approximately 2 km above and slightly further downstream, and these oscillations in u continue upwards through the model. From the potential temperature field (Fig. 18) one can see that the phase lines of these large amplitude waves (up to about 3 km) tilt upstream with height, characteristic of upward-propagating gravity waves. Where these waves reach the model's tropopause it appears that one has started to overturn and formed a 'jump-like' feature with a vertically orientated isentrope. This jump is produced by the action of the convective adjustment on the breaking wave, and also by the vertical diffusion, which tries to remove the instability associated with the very low Richardson numbers in this area (Fig. 22). It is associated with strong shear in the horizontal wind field, and also in the vertical velocity field (Fig. 21), with a minimum of -15 cm s^{-1} and a nearby maximum of 7 cm s^{-1} actually in the jump. The vertical velocity field near the mountain shows much more assymmetry than the S.G. model's, associated with the strong downslope wind (minimum $w \simeq -24$ cm s^{-1}), and it also shows up the waves downstream of the mountain. The along-mountain wind (v) similarly shows up these waves (Fig. 19), superimposed on the two main vortices seen in the results from the S.G. model (Fig. 14).

6. Discussion

The features discussed in section 5(a) concerning the S.G. model, especially the sharper surface front and low level vertical velocity maximum, seem to agree quite well with detailed analyses of cold fronts made by both Ogura and Portis [9] and Sanders [10]. The seemingly spurious bump in the isentropes and associated vertical velocity maximum and minimum in the P.E. model may be associated with internal gravity waves, whose origin is in the geostrophic adjustment process as the front collapses. Lee and Peltier [11] suggest that such waves can initiate squall line development ahead of a cold front. In their analysis a maximum surface pressure fluctuation of 5 mb was computed, and here we observe a pressure fluctuation in the P.E. model of 2.0 mb with a period of about 2 hours. Thus the P.E. model may be correct in producing these waves here, but their horizontal scale seems too large. The S.G. model, which cannot support these gravity waves, seems to produce a better large scale solution with more realistic fields and a tighter front.

The results from the P.E. model for the mountain case described in section 5(b) show some similarity to another case (shown in [4]) run from initial data taken from observations over the Alps with somewhat higher static stability and a higher mountain (2 km). In that case a very strong downslope wind was produced, together with an associated large hydraulic jump just downstream of the mountain. Here, with much lower static stability in the troposphere, there still seems to be a tendency to form a jump-type feature (similar to that formed near the tropopause) just

downstream of the mountain, where the isentropes are almost vertical and there is a large area with $R_i < 0.6$ (Fig. 22), although R_i has not fallen to the critical value of 0.25.

The time-mean of the pressure drag over the mountain $(\frac{1}{L_{mtn}} \sum_{i=1}^{N_{mtn}} (P^*_i \Delta h_i)$, where the length scale L_{mtn} is taken as the total width of the mountain and the sum is over the N_{mtn} grid-lengths across the mountain), calculated for the P.E. model, is 0.75 N m^{-2}, which is similar to values that have been observed over mountain ranges but with much stronger flows [12]. This value for the drag oscillates greatly in time between 0.02 and 1.5 N m^{-2} with a period of about 3 hours, associated with an oscillation in the surface pressure of about 5 mb, resembling a sloshing to and fro in the model. This is related to the large amount of wave activity in the P.E. model (produced despite the inclusion of a zone of increased horizontal diffusion near the top of the model), which is not seen in real situations of uniform flow over a mountain ridge with similar low static stability. There is also the tendency here, as in [4], to form waves on too large a horizontal scale — the scale of the mountain. As in [4] the over-response of the P.E. model here may be caused partially by the two-dimensionality of the model and the fact that all the flow is forced to cross the mountain rather than be deflected round it, as can happen in reality.

On the other hand, there are no gravity waves in the S.G. model and this is shown in the time-evolution of the pressure drag in this model. After firstly increasing steadily to a maximum value of 0.35 N m^{-2} after about 5 hours, associated with the higher θ values in the start vortex moving down the mountain side, and then decreasing approximately exponentially, it

tends to a constant value of 0.18 N m^{-2}. Also, the ageostrophic cross-mountain flow is mostly confined to the immediate vicinity of the mountain, as predicted theoretically. Although there is a little roughness in the otherwise uniform u-field above the mountain; and the ageostrophic component of the along-mountain wind (shown in Fig. 17) increases upwards from about ±2 m s^{-1} near the mountain surface to about ±5 m s^{-1} in the stratosphere, whereas it should be zero if the iteration was converging exactly. In the case shown in [4] where the mountain was higher there was a lot of noise generated by the iterative adjustment failing to converge, which was seen in the cross-mountain flow above the mountain. This was partly due to the convective adjustment and vertical diffusion being called in the larger unstable areas in that case and producing greater imbalances in the model, which the iteration scheme could not reduce effectively. Changes to the order of the steps in the integration scheme had little effect. The only difference between the model used in that case and the one here, is that P_* was not included in the stream function used in the adjustment step (equation (12)) in [4] as it is here.

Thus, overall in the two cases presented here, the S.G. model appears to give a more realistic large-scale solution, without the corrupting influence of the gravity waves produced in the P.E. model. Although the additional features produced in the P.E. model have counterparts in the real atmosphere, they seem to be exaggerated, especially the horizontal scale and extent of the gravity waves. Some of this is undoubtably due to the two-dimensionality of the model, but runs with the operational Fine Mesh model in [4] showed some similar features in this three-dimensional primitive equation model. So, from the cases shown here the S.G. model has

certain advantages, but in the more severe case shown in [4] the iteration did not converge adequately; and for this reason a fully implicit S.G. method has been formulated [13] and is now being tested.

References

[1] Cullen, M. J. P. 1983 Further solutions to the two-dimensional deformation model. Met O 11 Tech. note No. 163.

[2] Cullen, M. J. P. and Purser, R. J. 1984 An extended Lagrangian theory of semi-geostrophic frontogenesis. J. Atmos. Sci., 41, 1477-1497.

[3] Parrett, C. A. and Cullen M. J. P. 1984 Simulation of hydraulic jumps in the presence of rotation and mountains. Quart. J. Roy. Meteor. Soc., 110, 147-165.

[4] Cullen, M. J. P. and Parrett, C. A. 1987 Mountain wave generation by models of flow over synoptic scale orography. Quart. J. Roy. Meteor. Soc., to appear.

[5] Saker, N. J. 1975 An 11-layer general circulation model. Met O 20 Tech. Note No. II/30.

[6] Hoskins, B. J. and Bretherton, F. P. 1972 Atmospheric frontogenesis models: mathematical formulation and solution. J. Atmos. Sci., 29, 11-37.

[7] Cullen, M. J. P. 1983 Solutions to a model of a front forced by deformation. Quart. J. Roy. Meteor. Soc., 109, 565-573.

[8] Foreman, S. J. 1983 The numerical weather prediction model of the Met Office. Amer. Meteor. Soc., 6th Conference on N.W.P., Omaha, Nebraska, 96-101.

[9] Ogura, Y.and Portis, D. 1982 Structure of the cold front observed in SESAME-AVE III and its comparison with the Hoskins-Bretherton frontogenesis model. J. Atmos. Sci., 39, 2773-2792.

[10] Sanders, F. 1955 An investigation of the structure and dynamics of an intense surface frontal zone. J. Meteor., 12, 542-552.

[11] Ley, B. E. and Peltier, W. R. 1978 Wave generation and frontal collapse. J. Atmos. Sci., 35, 3-17.

[12] Hoinka, K. P. 1985 Observation of the airflow over the Alps during a foehn event. Quart. J. Roy. Meteor. Soc., 111, p 199-224.

[13] Cullen, M. J. P. and Parrett, C. A. 1986 Fully implicit Newton methods for accurate treatment of vertical atmospheric structure. WMO/IUGG International symposium on short- and medium-range numerical weather prediction, Tokyo, 4-8 August 1986. WMO/TD - No. 114.

List of figures

18. Results from the P.E. model after 24 hours: potential temperature field, contour interval = 2°C.

19. As 18, but along-mountain wind field, contour interval = 2 m s^{-1}.

20. As 18, but cross-mountain wind field, contour interval = 2 m s^{-1}.

21. As 18, but vertical velocity field, contour interval = 2 cm s^{-1}.

22. As 18, but the Richardson number, logarithmic contour interval.

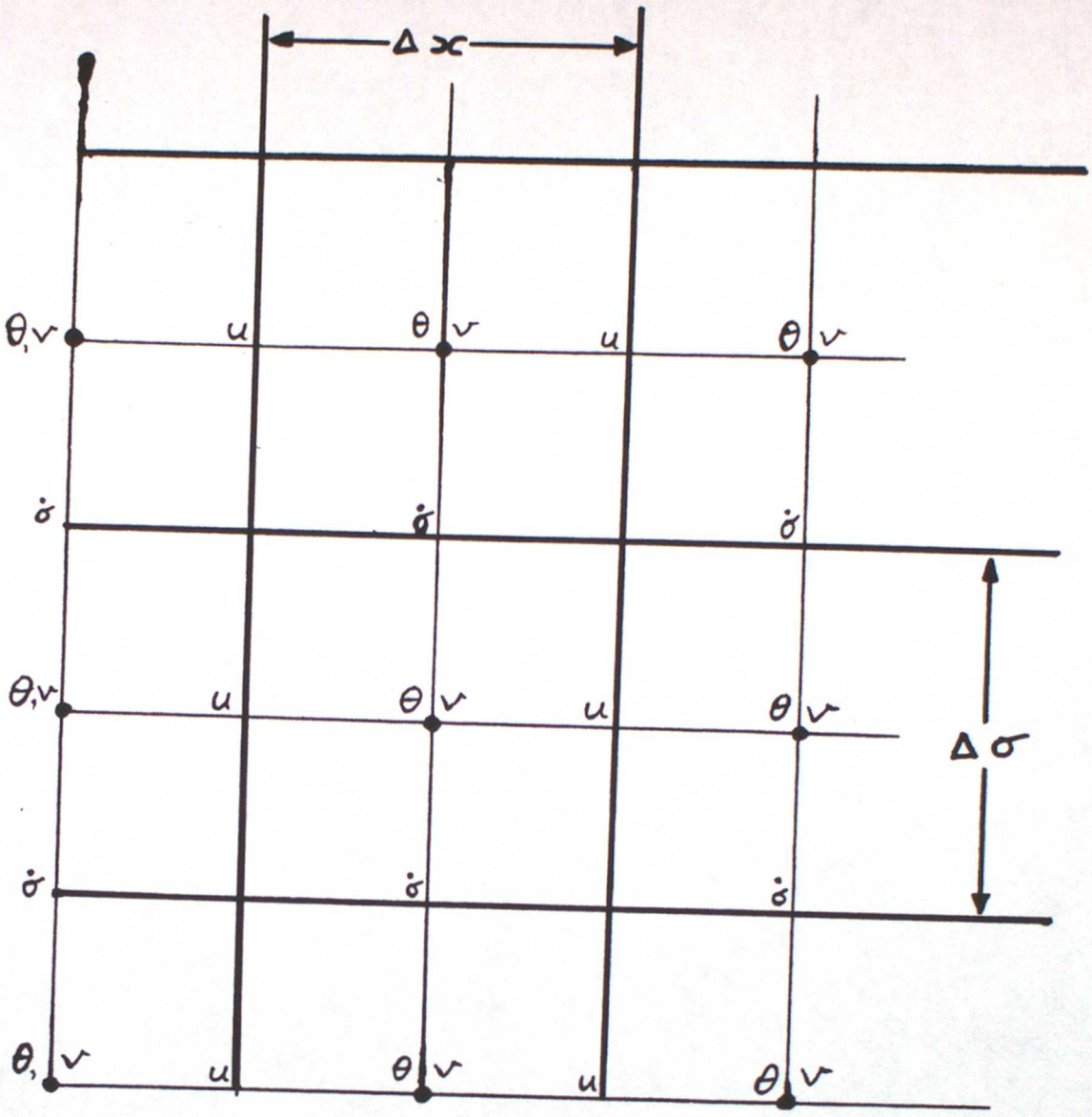

FIGURE 1.

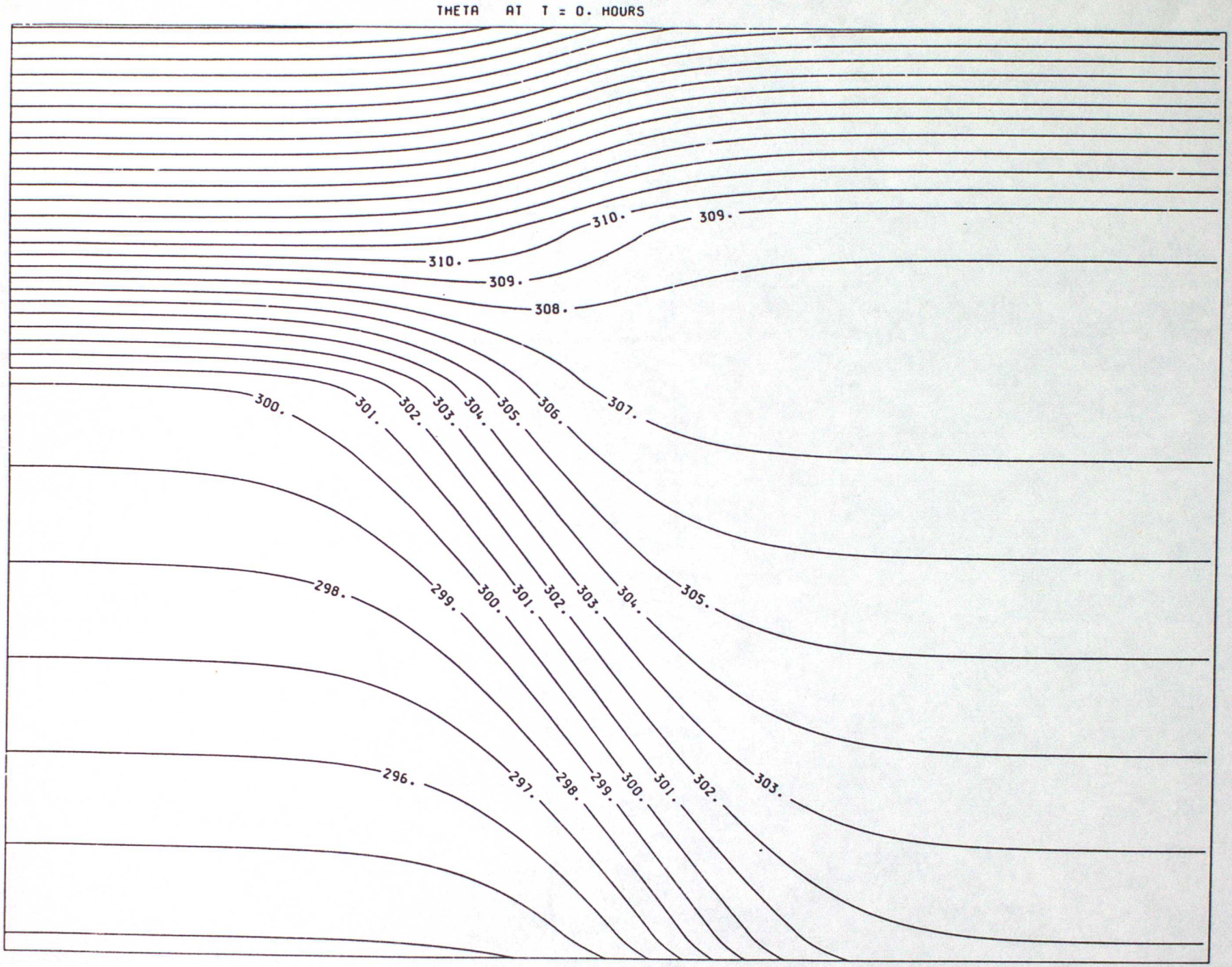
THETA AT T = 0. HOURS
310.
309.
310.
309.
308.
307.
306.
305.
304.
303.
302.
301.
300.
305.
304.
303.
302.
301.
300.
299.
298.
303.
302.
301.
300.
299.
298.
297.
296.

FIG. 2

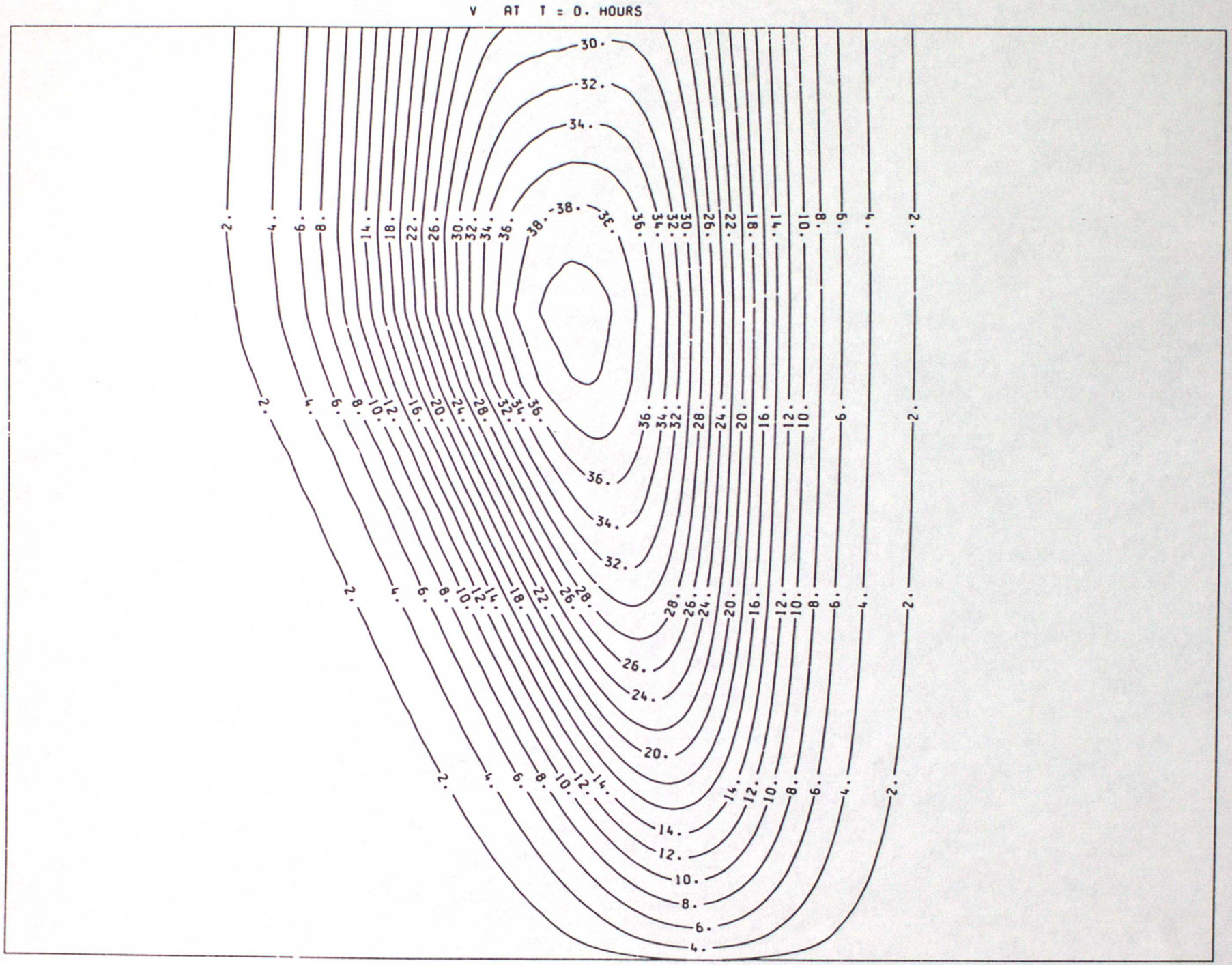

FIG. 3

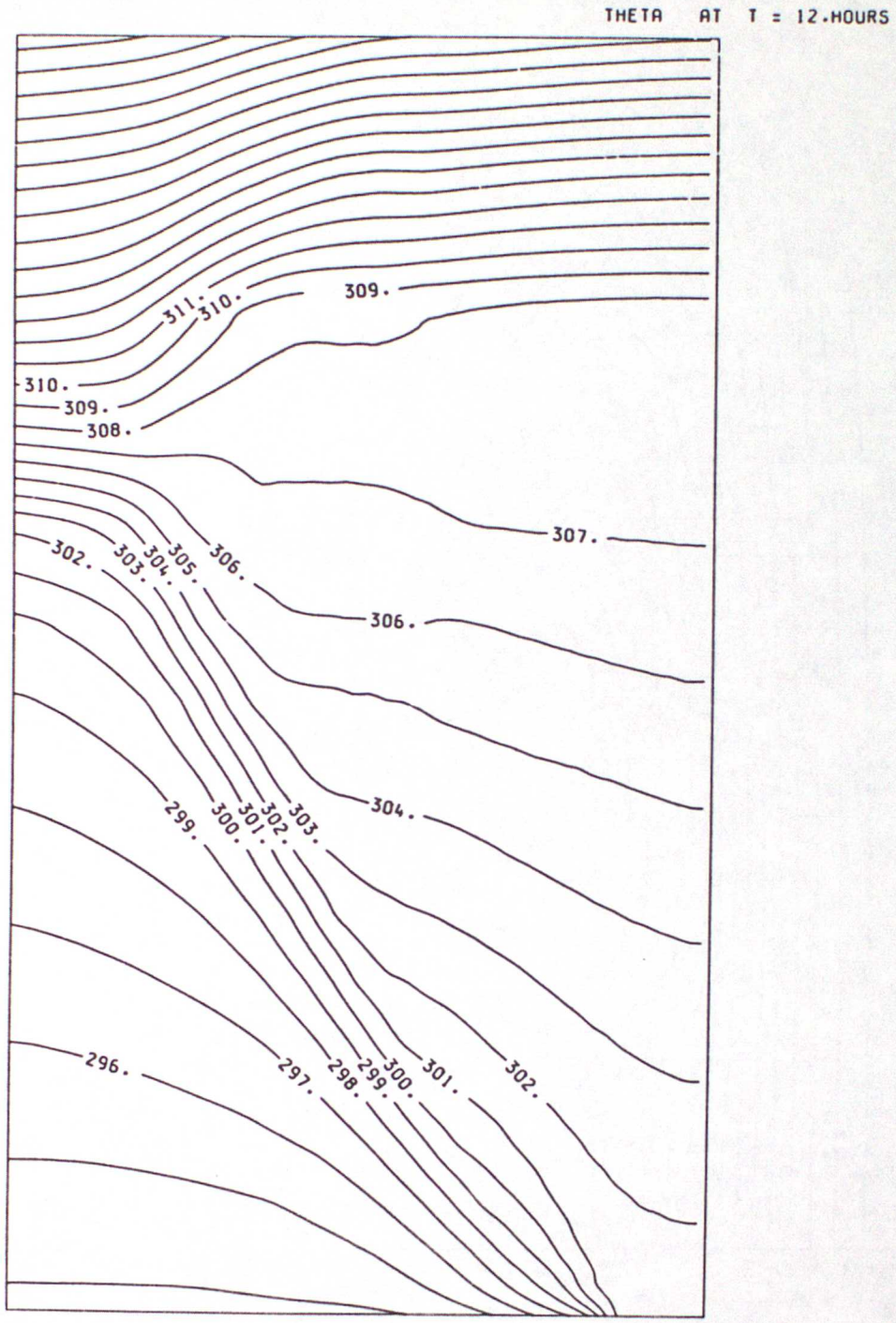
THETA AT T = 12.HOURS
311.
310.
309.
310.
309.
308.
307.
306.
306.
305.
304.
304.
303.
303.
302.
302.
302.
301.
301.
300.
300.
299.
299.
298.
297.
296.

Fig. 4

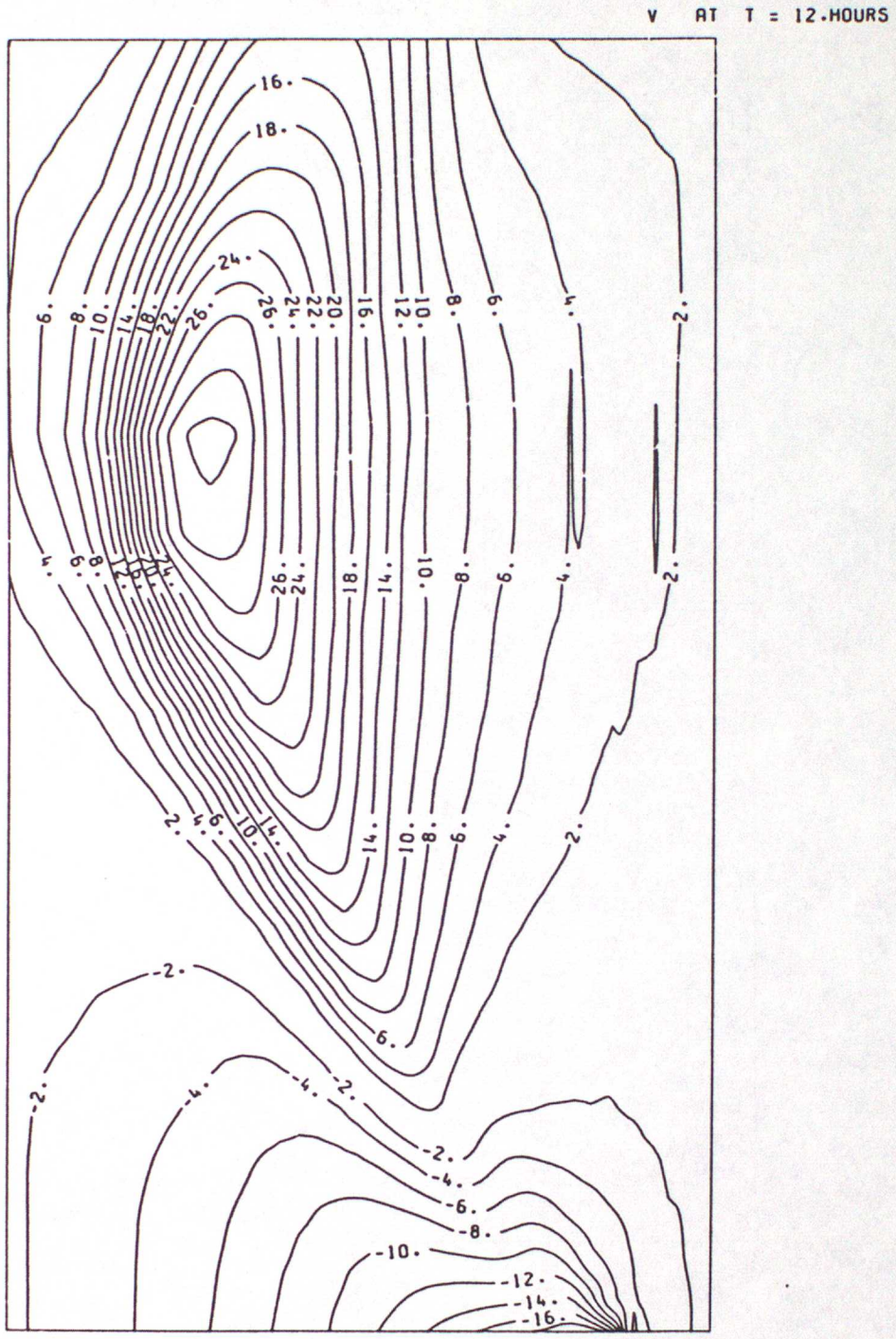

Fig. 5

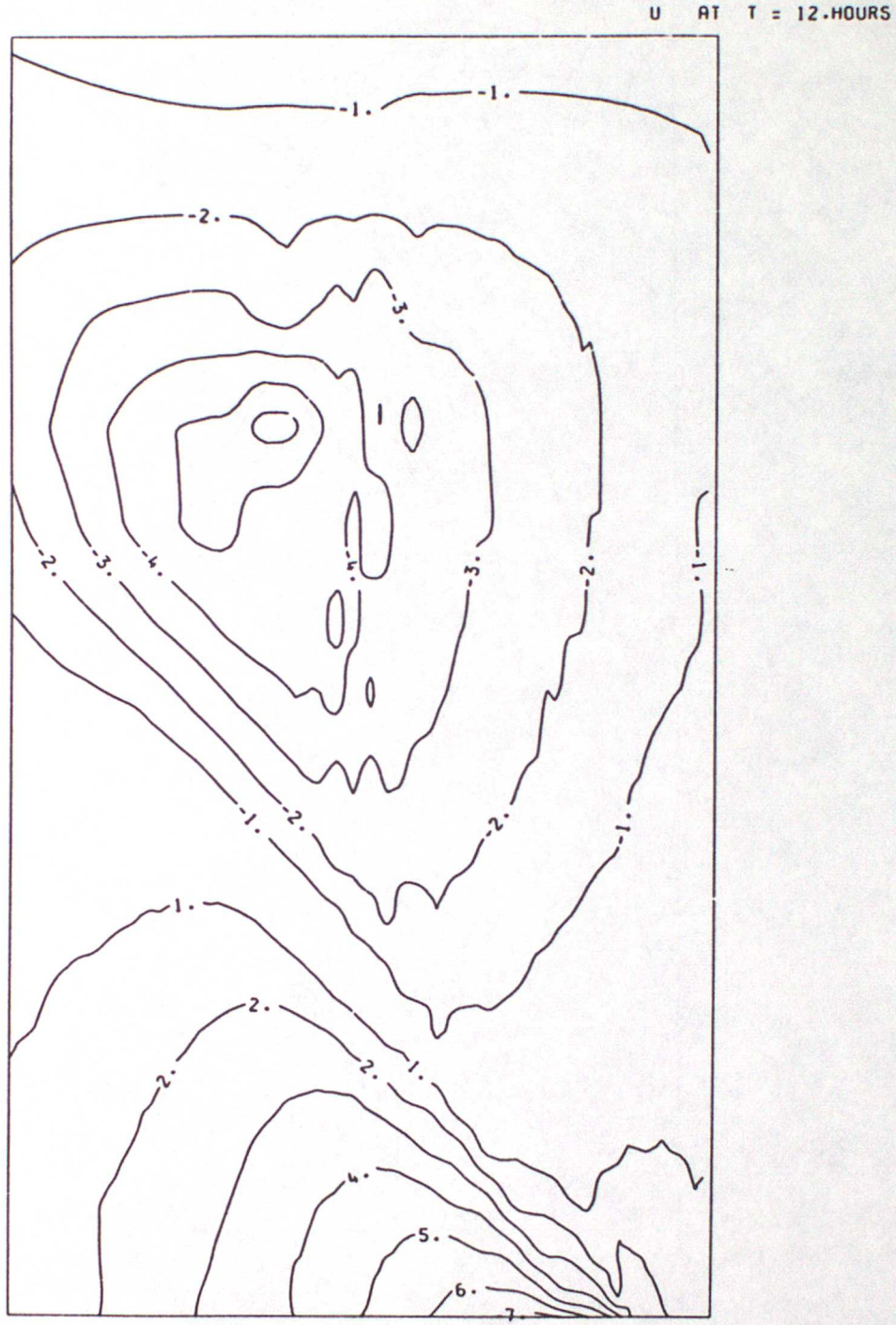

Fig. 6

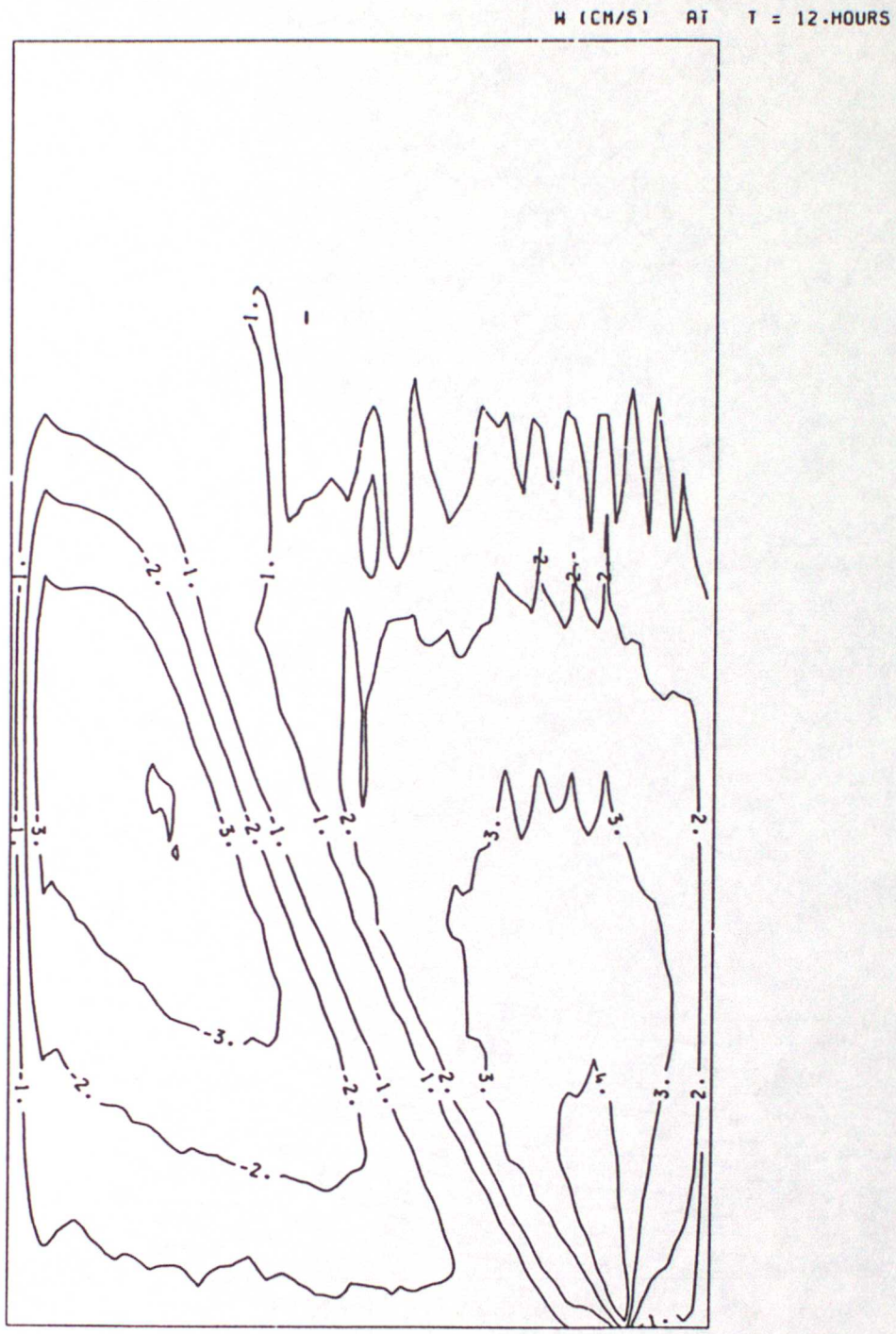

Fig. 7

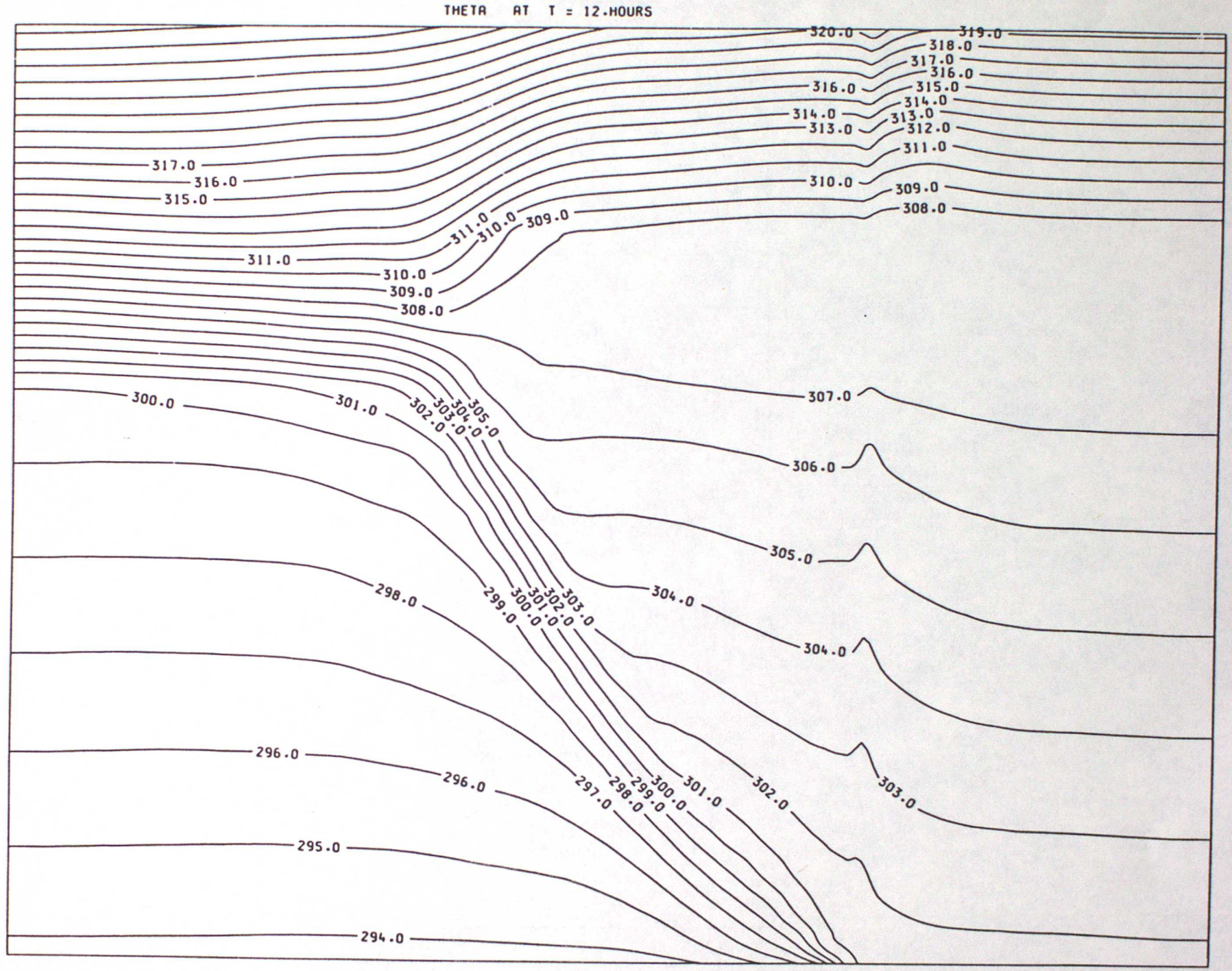
THETA AT T = 12.HOURS
320.0
319.0
318.0
317.0
316.0
316.0
315.0
314.0
314.0
313.0
313.0
312.0
311.0
317.0
316.0
315.0
311.0
310.0
309.0
308.0
311.0
310.0
309.0
308.0
307.0
306.0
305.0
304.0
304.0
303.0
300.0
301.0
302.0
303.0
304.0
305.0
298.0
299.0
300.0
301.0
302.0
303.0
296.0
296.0
297.0
298.0
299.0
300.0
301.0
302.0
303.0
295.0
294.0

Fig. 8

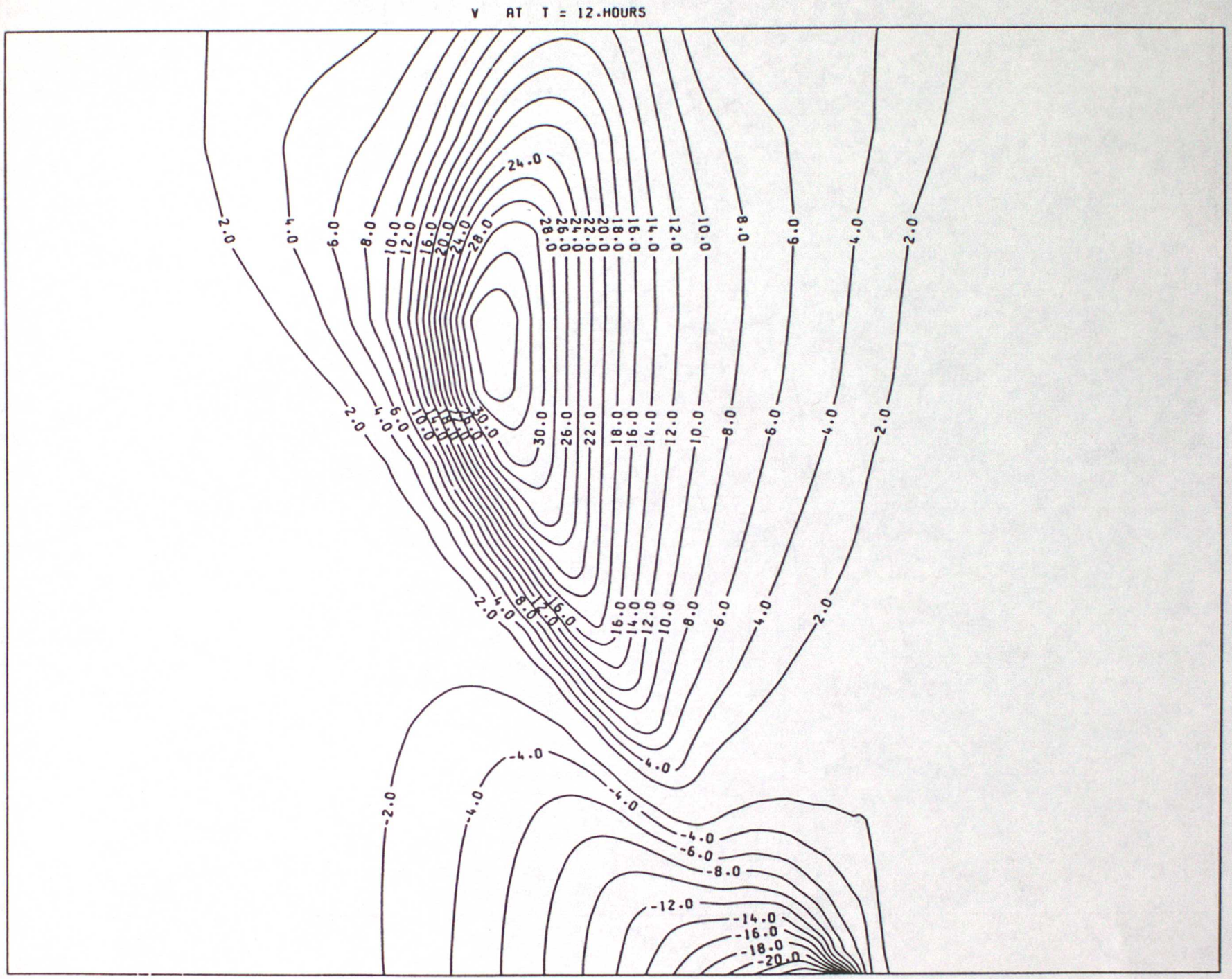

Fig. 9

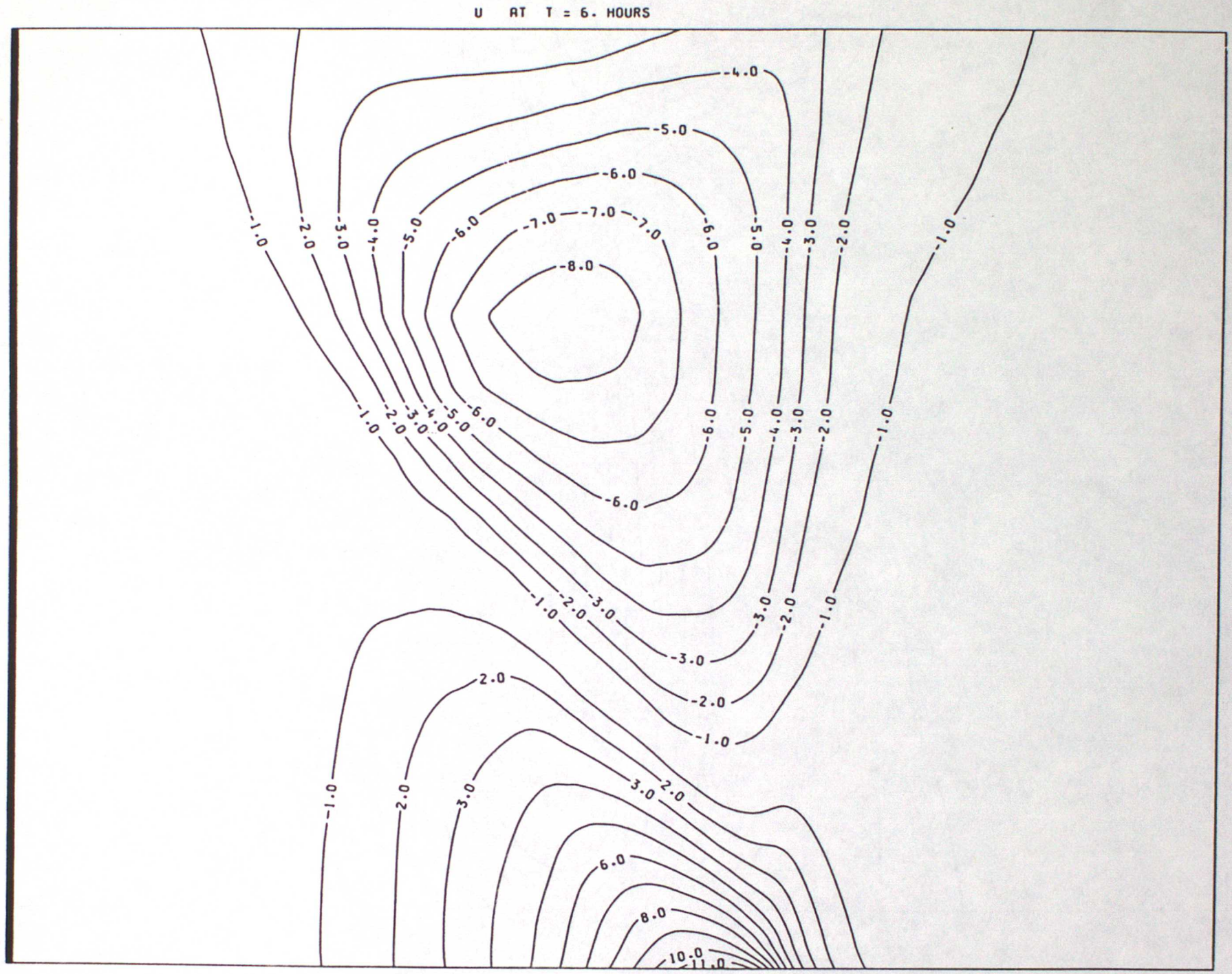

Fig. 10 (a)

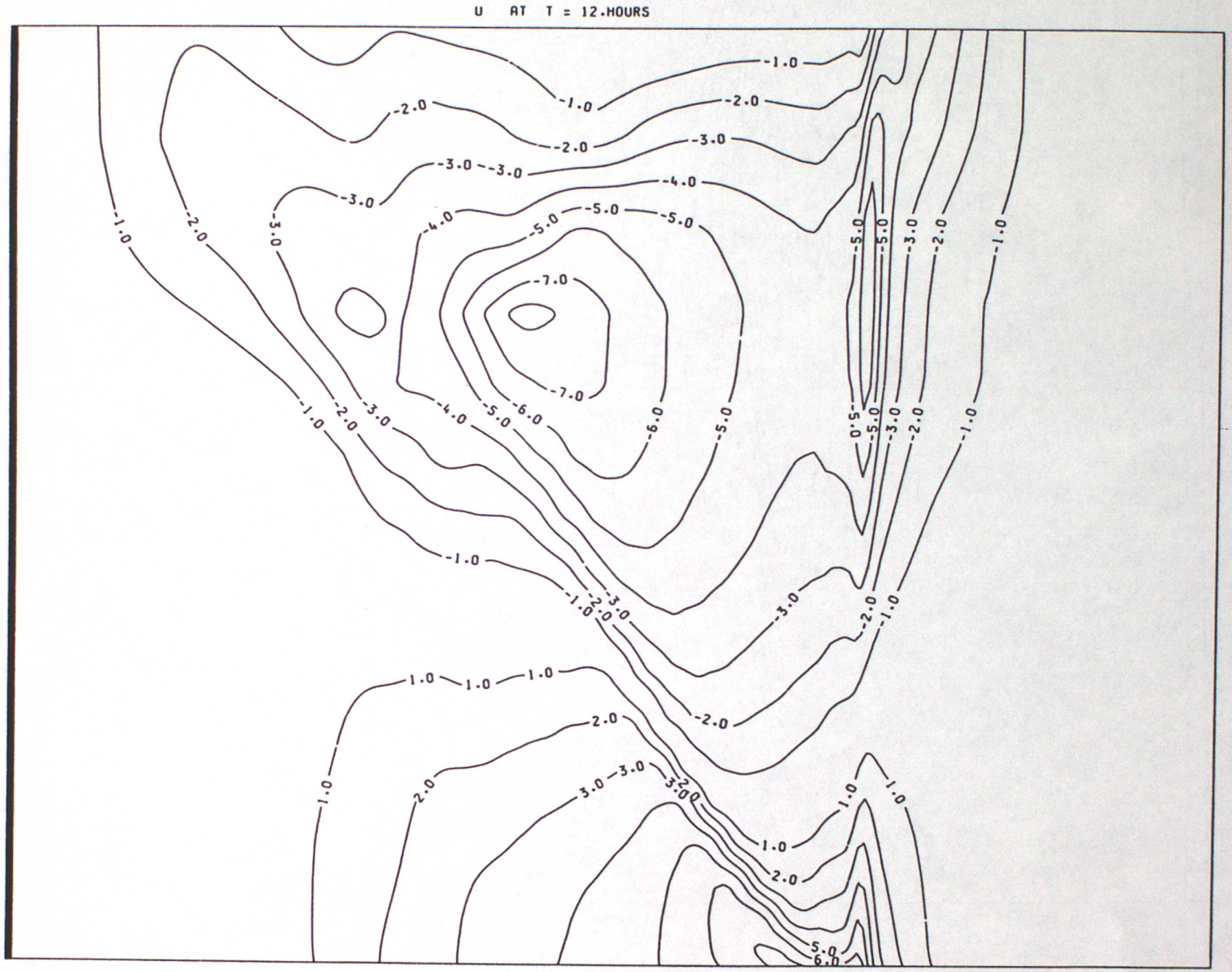

Fig. 10(b)

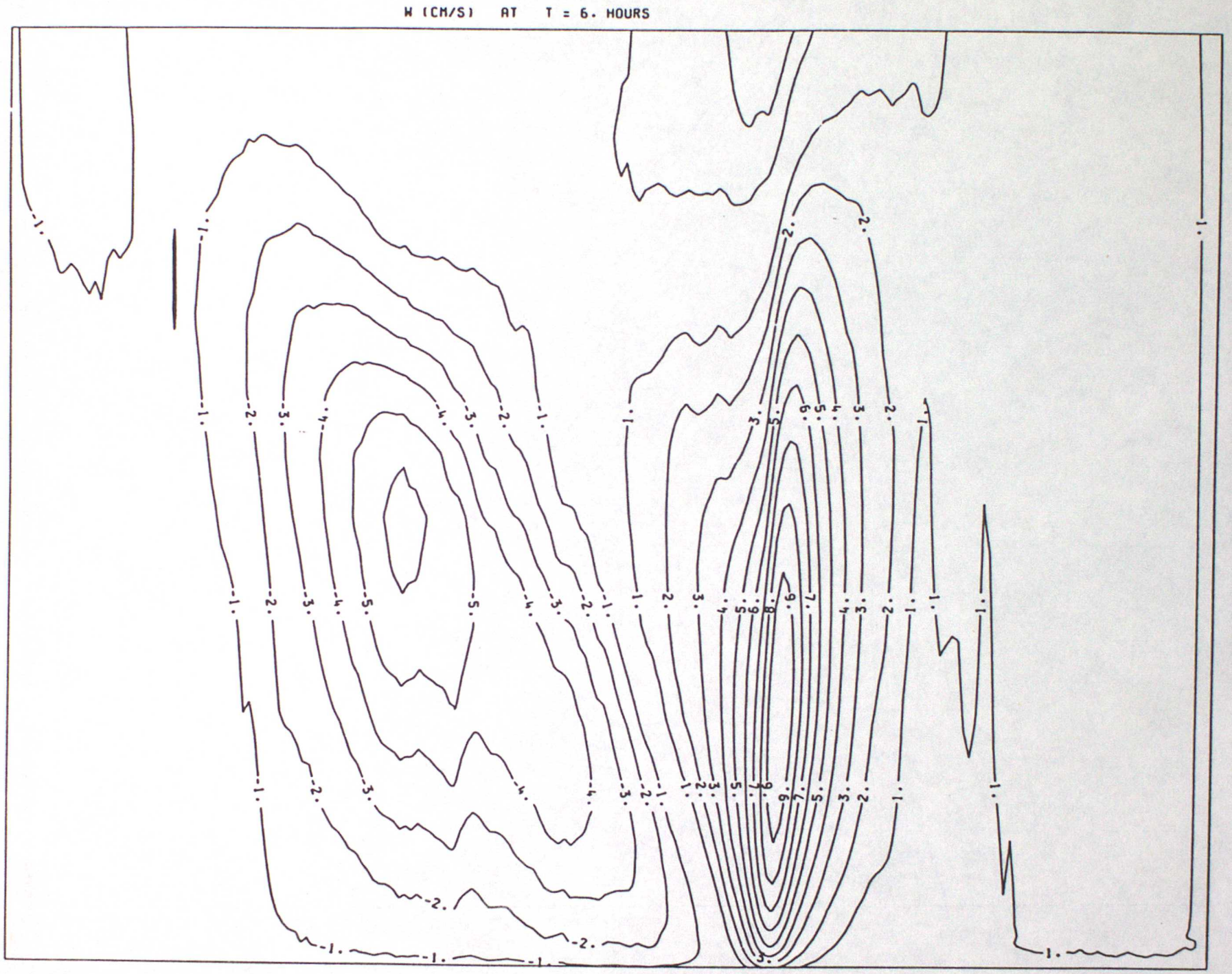

Fig. 11(a)

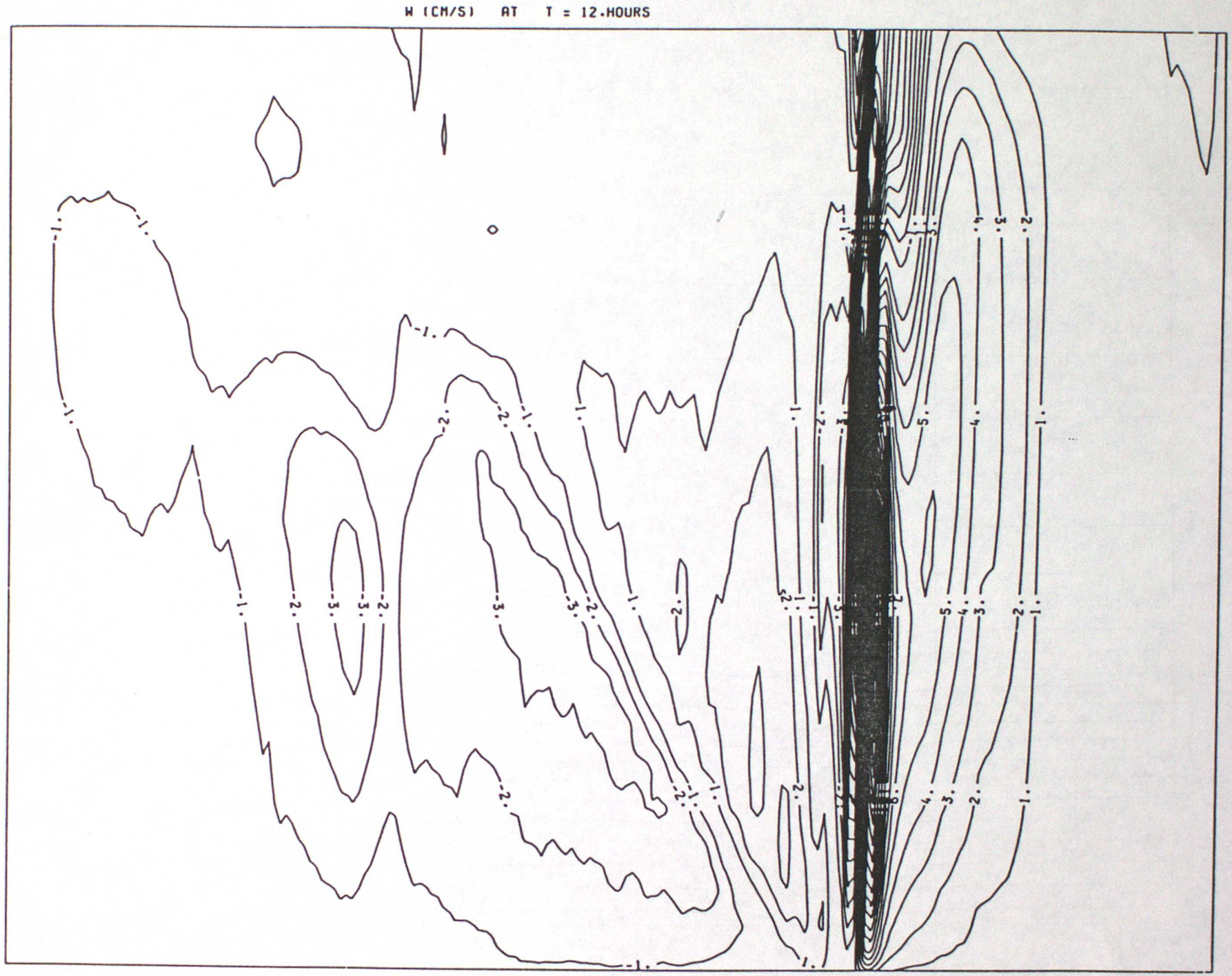

FIG. 11 (b)

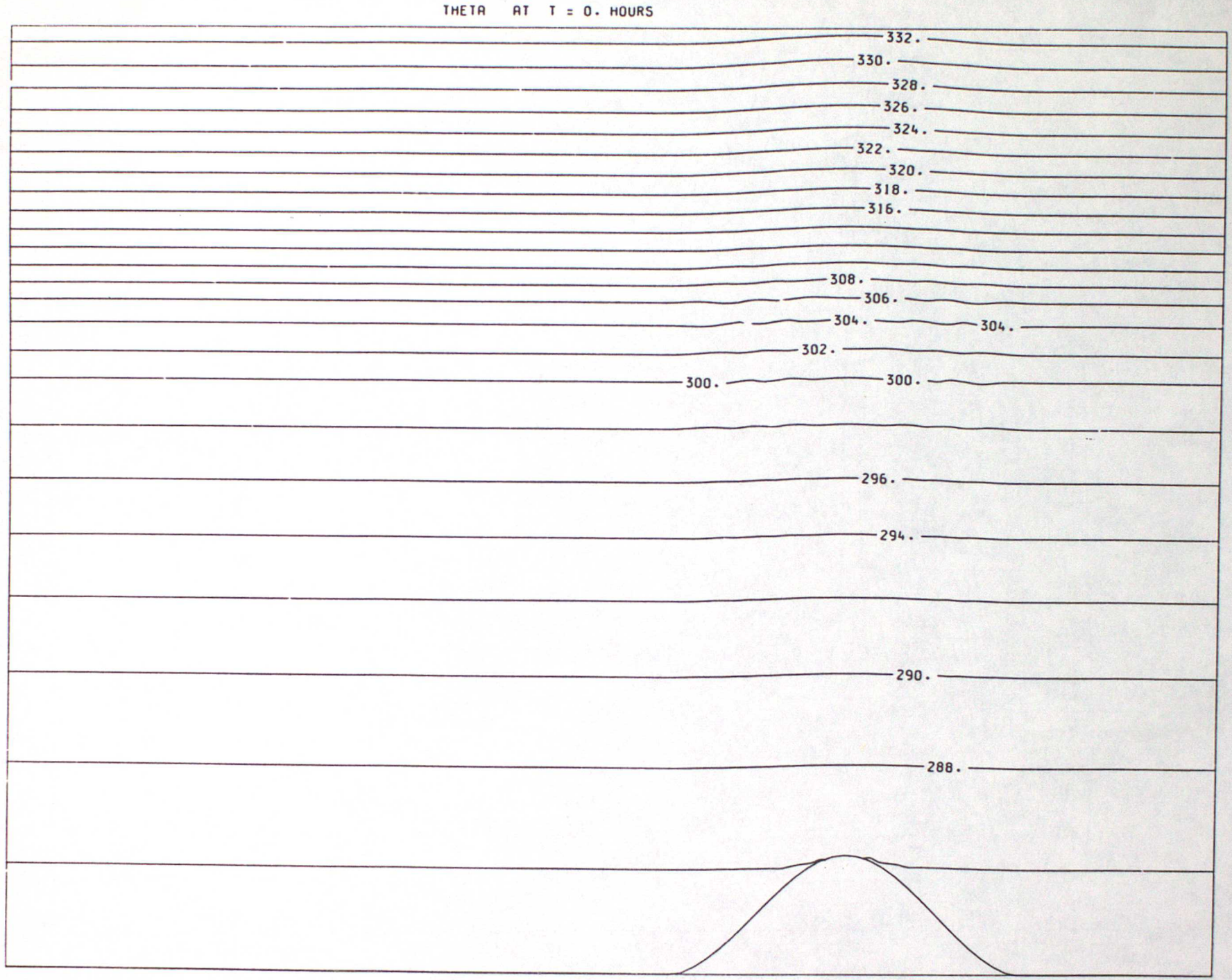
THETA AT T = 0. HOURS
332.
330.
328.
326.
324.
322.
320.
318.
316.
308.
306.
304.
304.
302.
300.
300.
296.
294.
290.
288.

Fig. 12

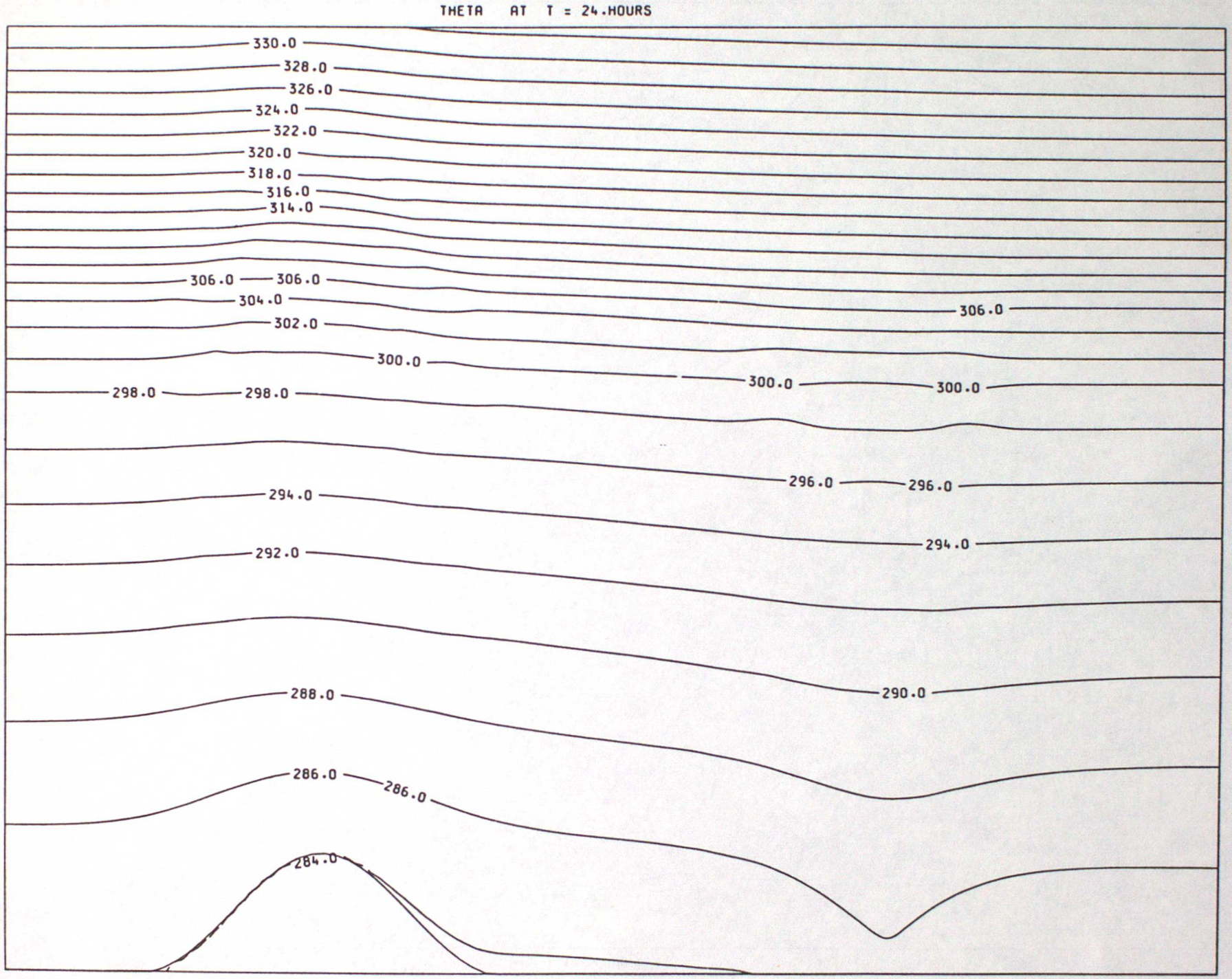
THETA AT T = 24.HOURS
330.0
328.0
326.0
324.0
322.0
320.0
318.0
316.0
314.0
306.0
306.0
304.0
306.0
302.0
300.0
300.0
298.0
298.0
300.0
296.0
296.0
294.0
294.0
292.0
290.0
288.0
286.0
286.0
284.0

FIG. 13

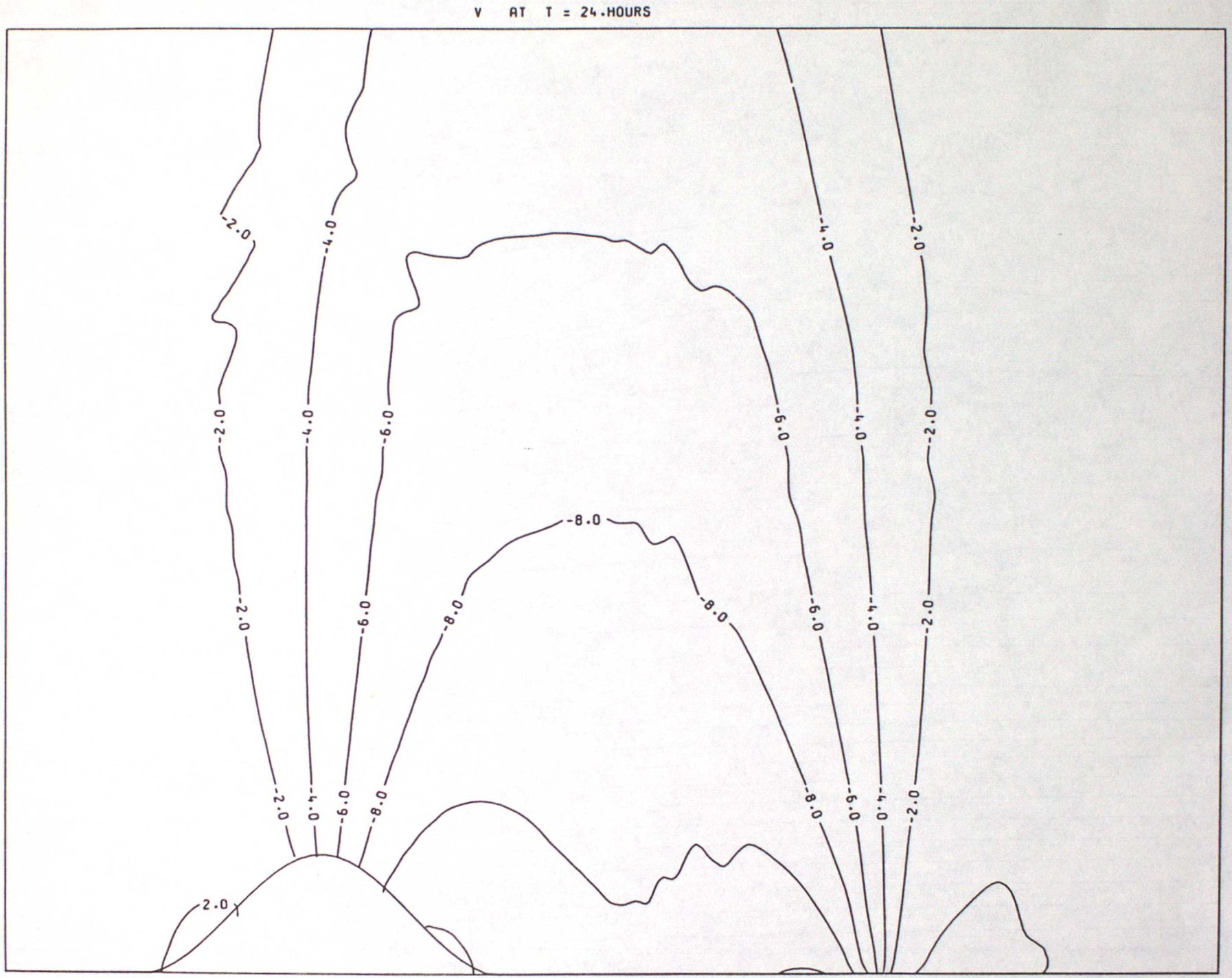

FIG. 14

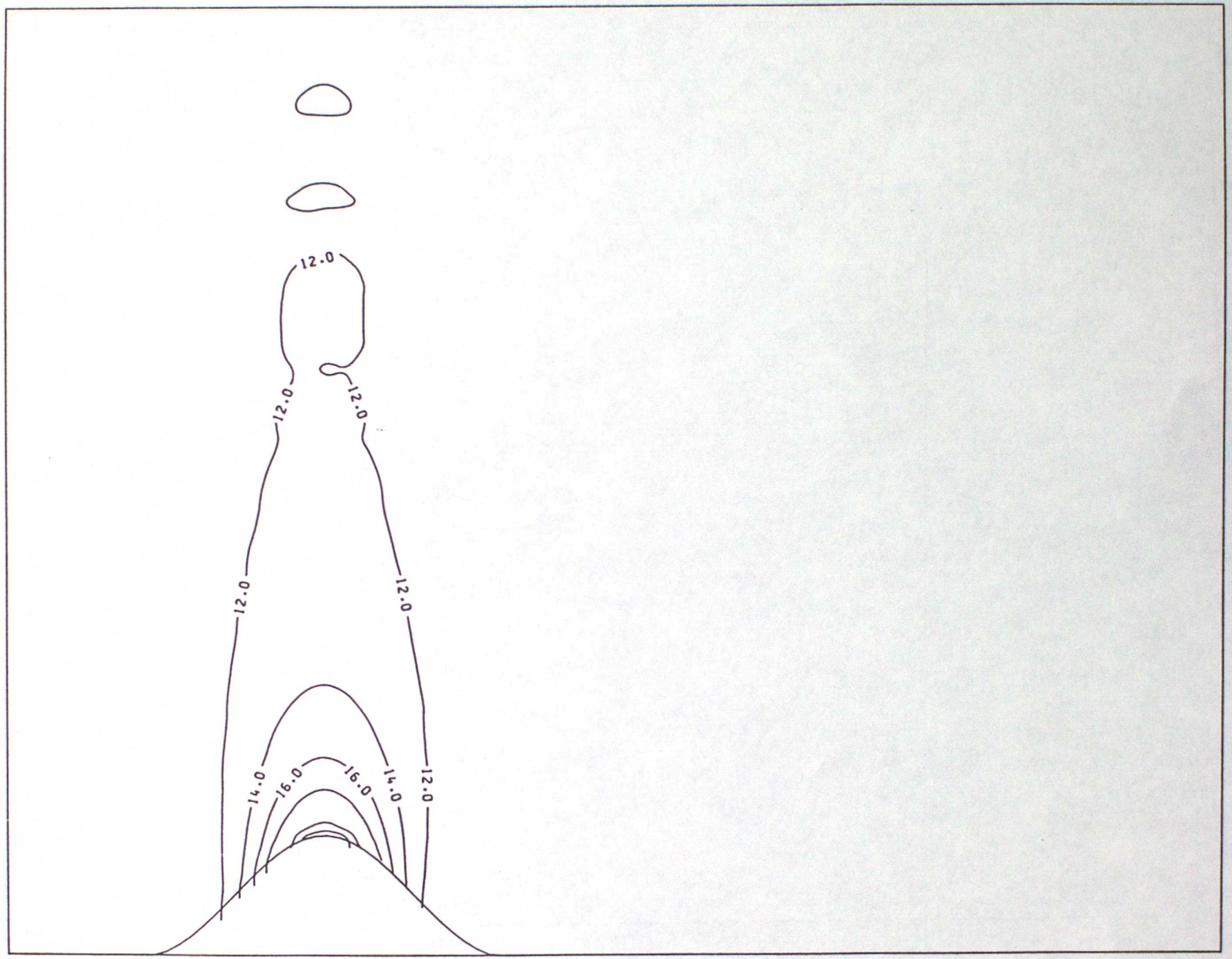

FIG. 15

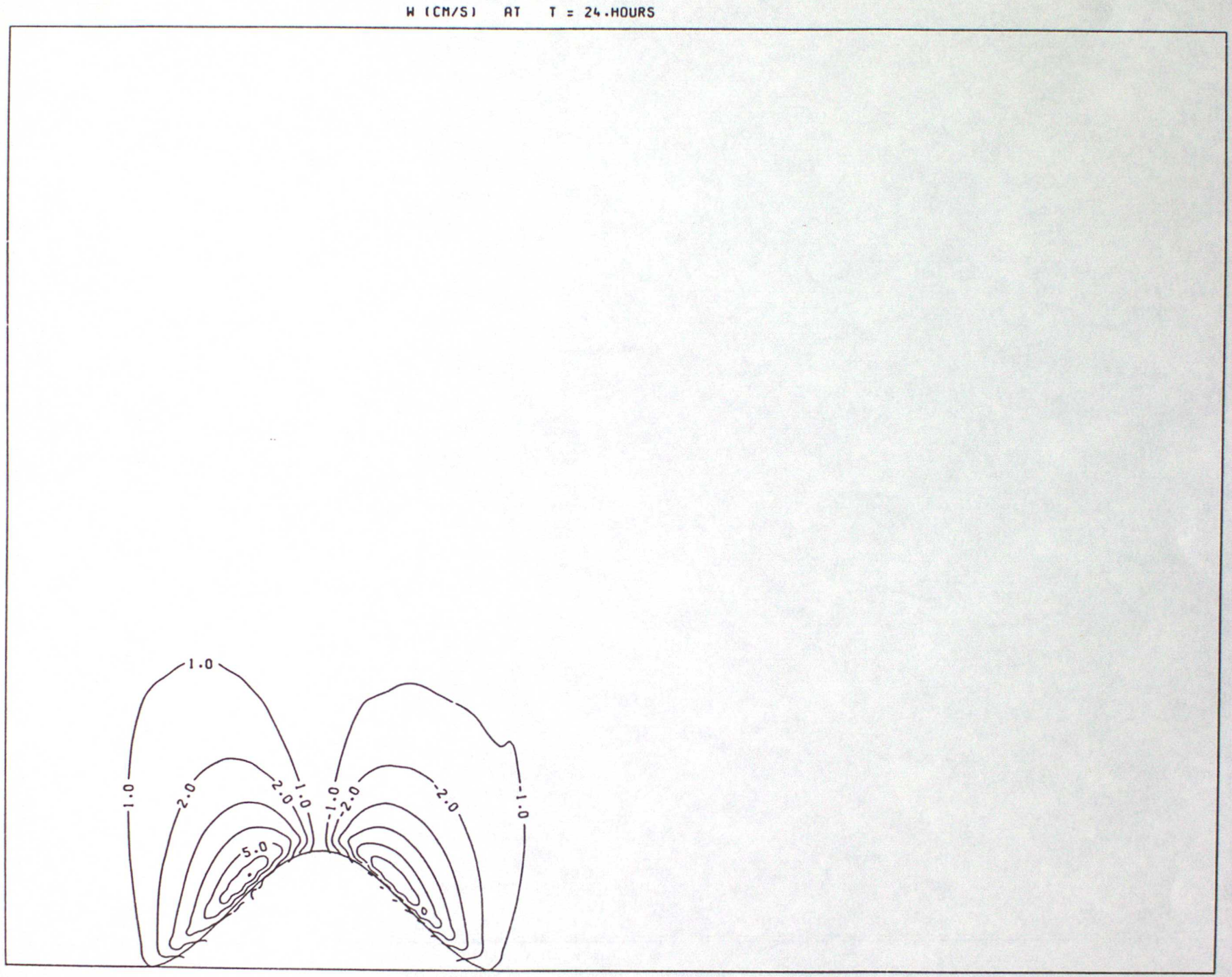

FIG. 16

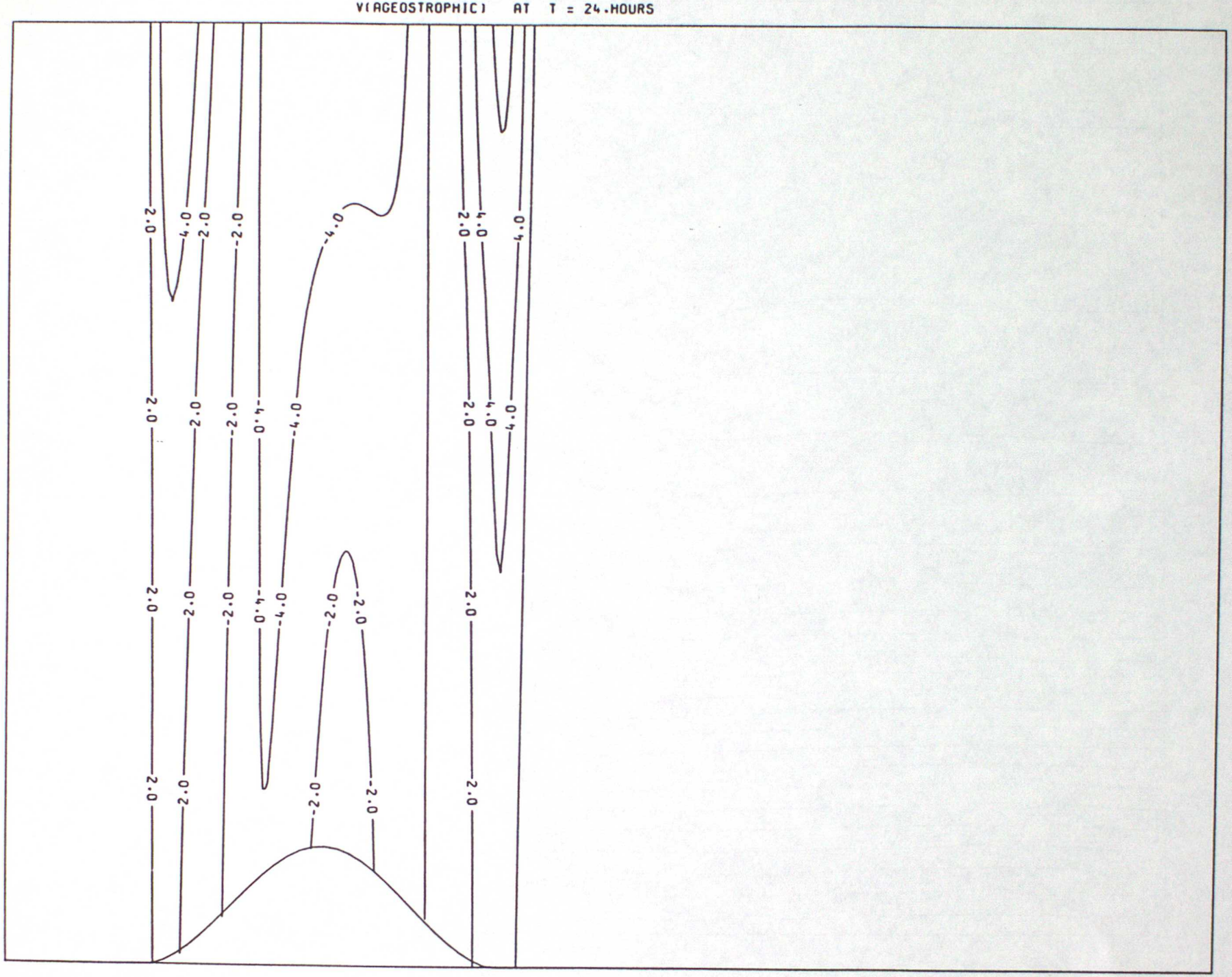

Fig. 17

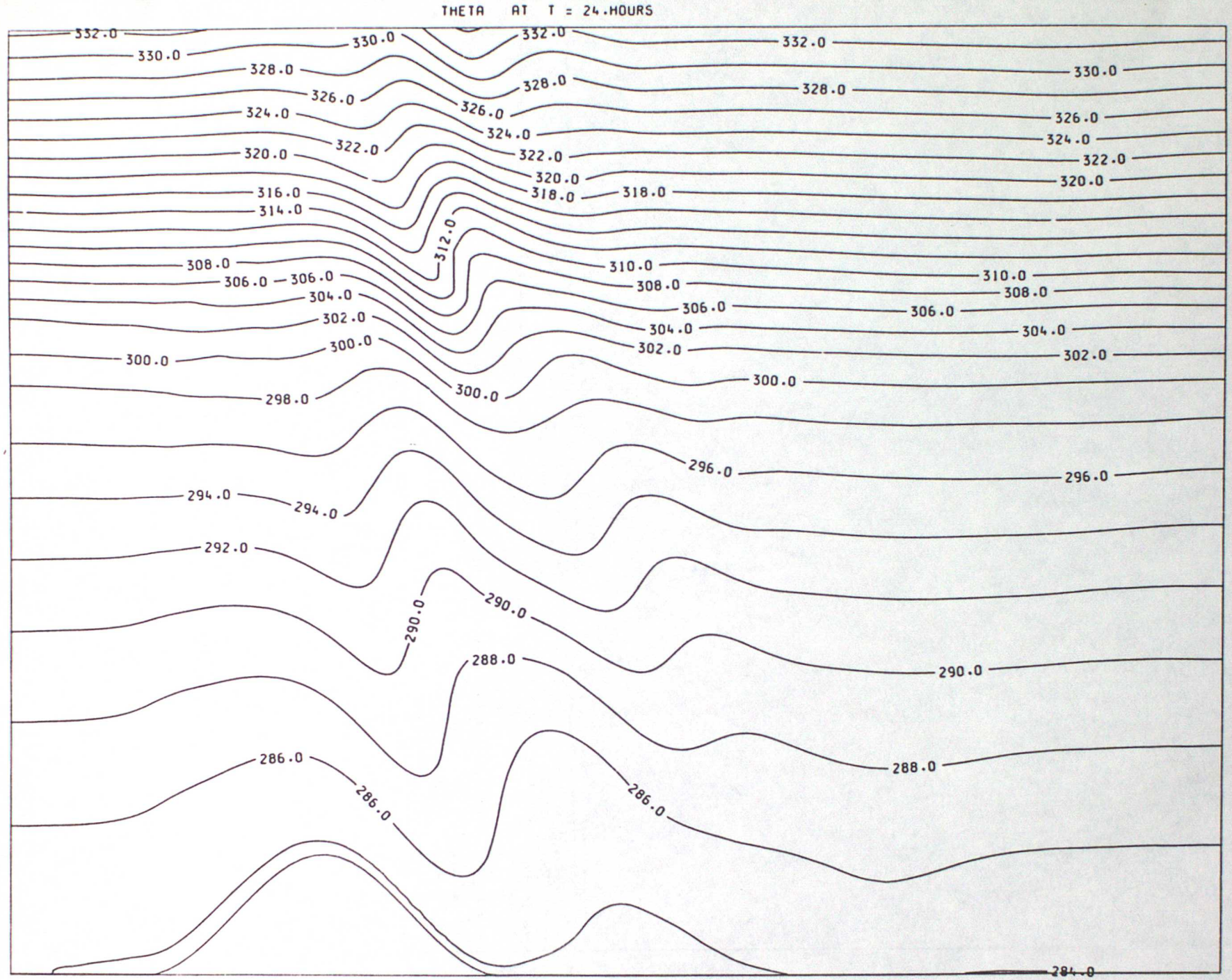
THETA AT T = 24.HOURS
332.0
330.0
328.0
326.0
324.0
322.0
320.0
318.0
316.0
314.0
312.0
310.0
308.0
306.0
304.0
302.0
300.0
298.0
296.0
294.0
292.0
290.0
288.0
286.0
284.0

FIG. 18

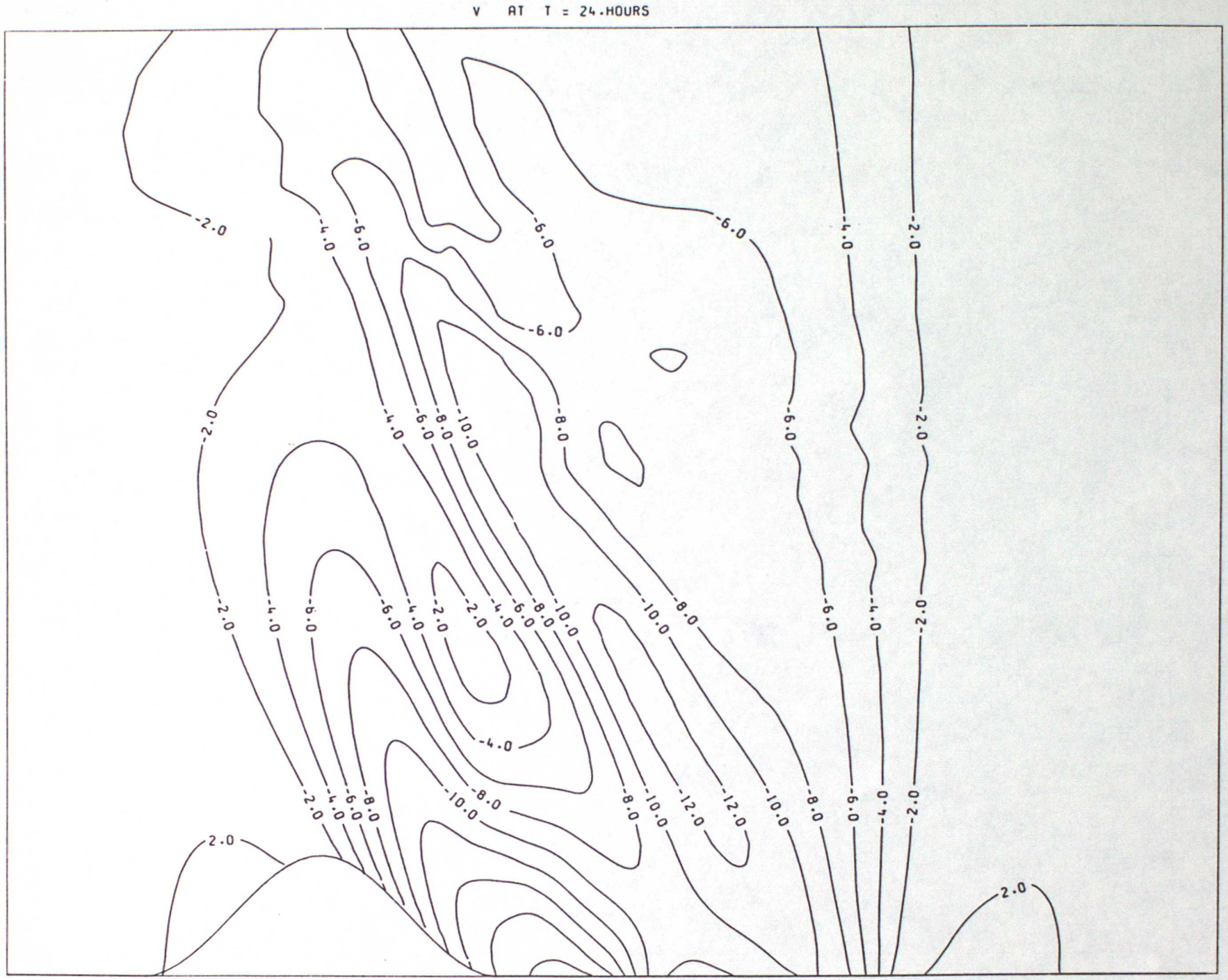

Fig. 19

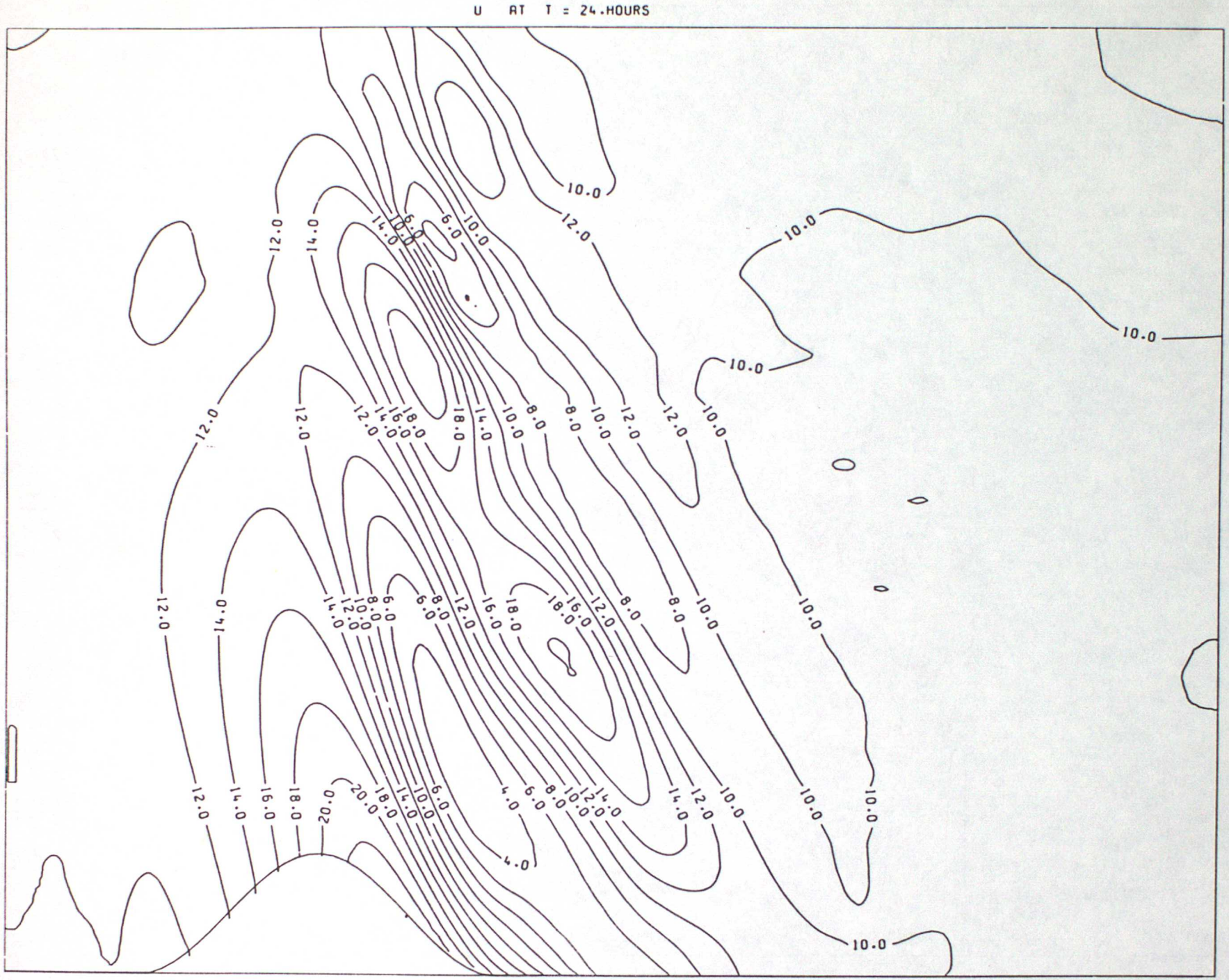

Fig. 20

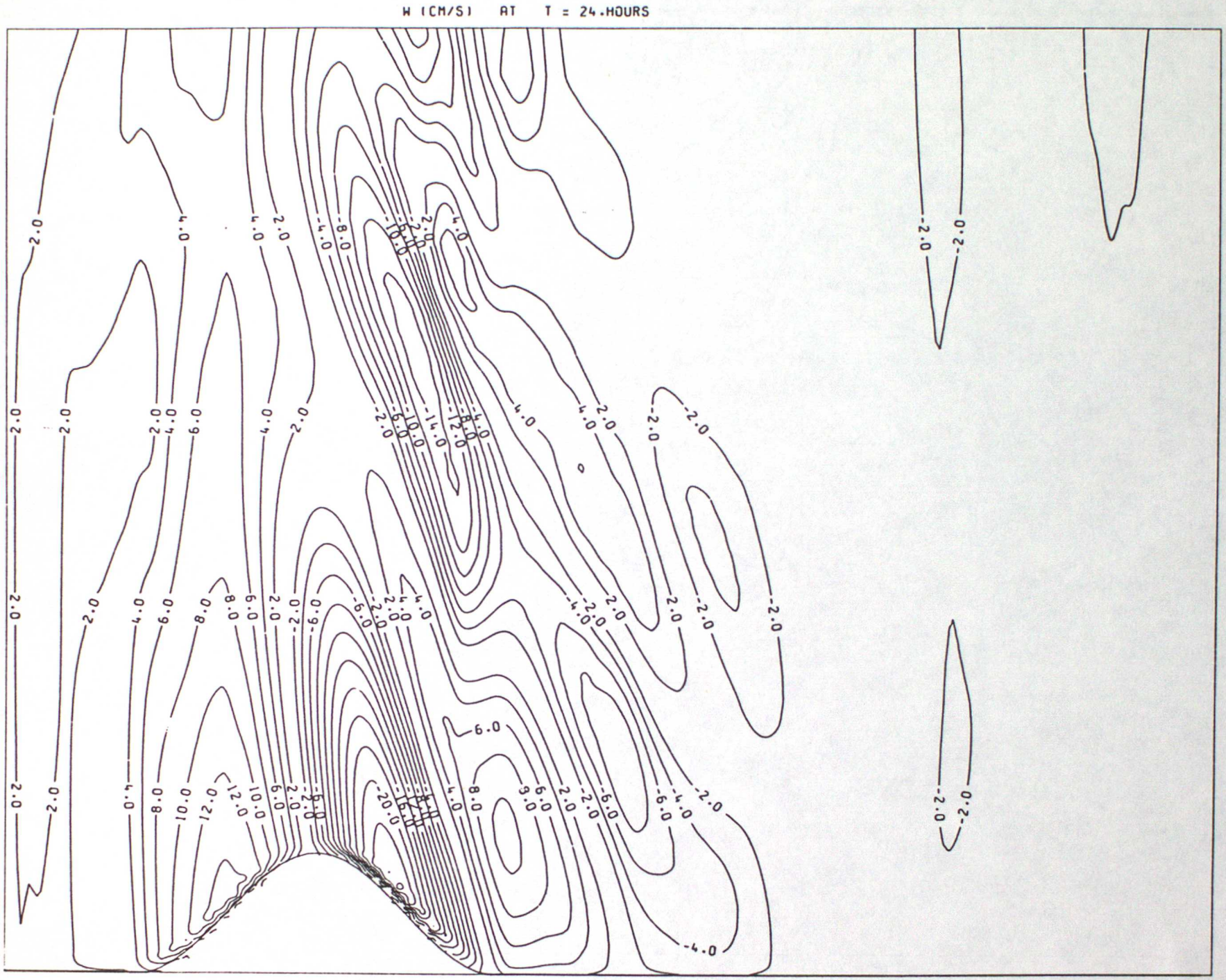

FIG. 21

RICHARDSON NO. AT T = 24.

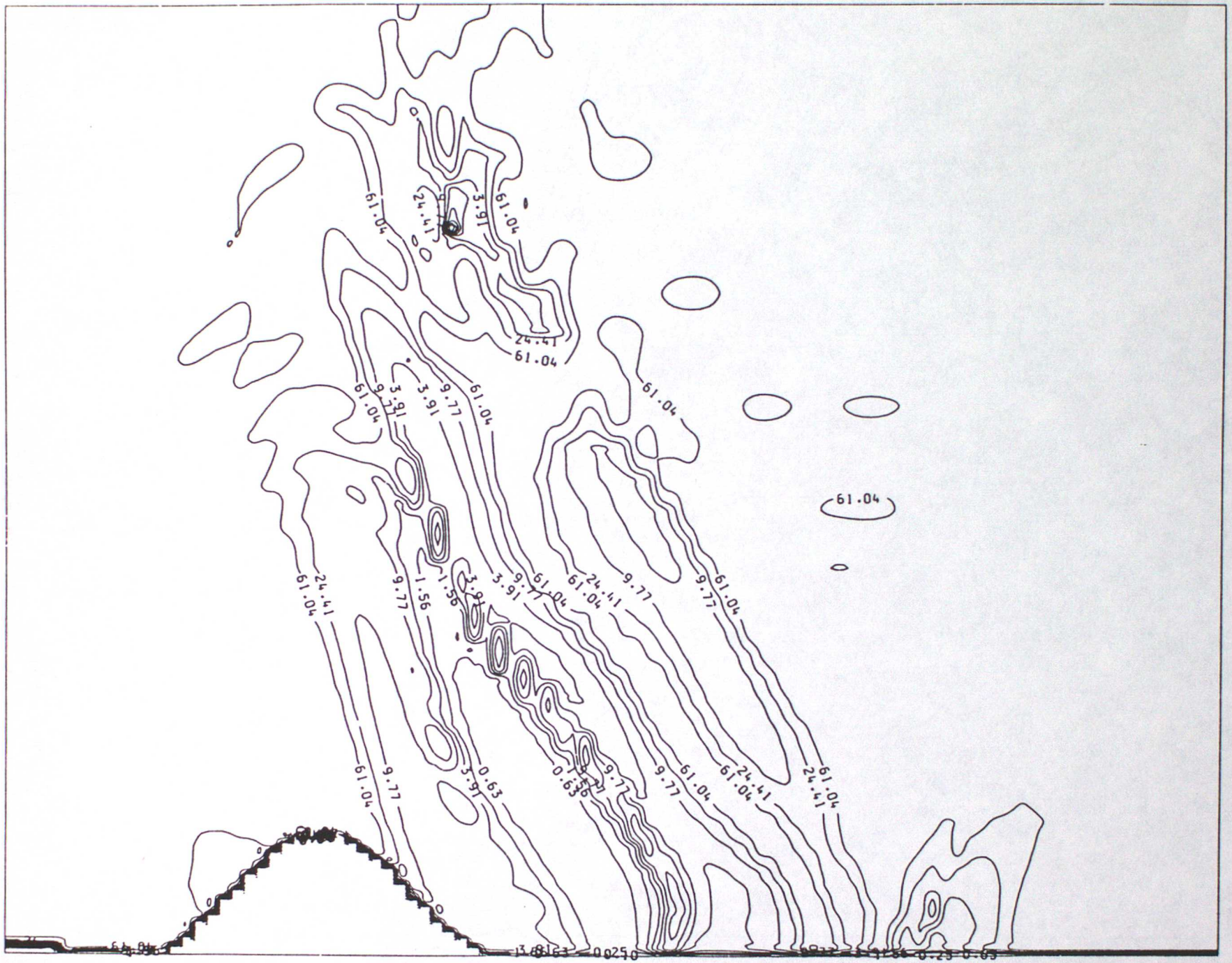

Fig. 22